Planetary and Space Science 126 (2016) 34–48

Contents lists available at ScienceDirect

Planetary and Space Science

journal homepage: www.elsevier.com/locate/pss

IR heterodyne spectrometer MILAHI for continuous monitoring observatory of Martian and Venusian atmospheres at Mt. Haleakalā, Hawaii

Hiromu Nakagawa [a,*], Shohei Aoki [b], Hideo Sagawa [c], Yasumasa Kasaba [a], Isao Murata [a], Guido Sonnabend [d], Manuela Sornig [e], Shoichi Okano [f], Jeffrey R. Kuhn [f], Joseph M. Ritter [f], Masato Kagitani [a], Takeshi Sakanoi [a], Makoto Taguchi [g], Kosuke Takami [a]

[a] Department of Geophysics, Graduate School of Science, Tohoku University, 6-3 Aramaki Aza Aoba, Aoba-ku, Sendai, Miyagi 980-8578, Japan
[b] Istituto di Astrofisica e Planetologia Spazialia (IASP), Istituto Nazionale di AstroFisica (INAF), Via del Fosso del Cavaliere 100, 00133 Roma, Italy
[c] Faculty of Science, Kyoto Sangyo University, Motoyama, Kamigamo, Kita-ku, Kyoto, 603-8555 Japan
[d] Radiometer Physics GmbH, Birkenmaar Str., 10, 53340 Meckenheim, Germany
[e] German Aerospace Center (Deutsches Zentrum fur Luft –und Raumfahrt), Konigswinterer Str., 522-524, 53227 Bonn, Germany
[f] Institute for Astronomy, University of Hawaii, Advanced Technology Research Center, 34 Ohia Ku St., Pukalani, HI, 96768 USA
[g] Rikkyo University, 3-34-1, Nishi-Ikebukuro, Toshima-ku, Tokyo, 171-8501 Japan

ARTICLE INFO

Article history:
Received 9 December 2015
Received in revised form
7 April 2016
Accepted 7 April 2016
Available online 20 April 2016

Keywords:
Spectroscopy
Infrared
Planetary atmospheres
High spectral resolution
Heterodyne

ABSTRACT

A new Mid-Infrared Laser Heterodyne Instrument (MILAHI) with $> 10^6$ resolving power at 7–12 μm was developed for continuous monitoring of planetary atmospheres by using dedicated ground-based telescopes for planetary science at Mt. Haleakalā, Hawaii. Room-temperature-type quantum cascade lasers (QCLs) that cover wavelength ranges of 7.69–7.73, 9.54–9.59, and 10.28–10.33 μm have been newly installed as local oscillators to allow observation of CO_2, CH_4, H_2O_2, H_2O, and HDO. Modeling and predictions by radiative transfer code gave the following scientific capabilities and measurement sensitivities of the MILAHI. (1) Temperature profiles are achieved at altitudes of 65–90 km on Venus, and the ground surface to 30 km on Mars. (2) New wind profiles are provided at altitudes of 75–90 km on Venus, and 5–25 km on Mars. (3) Direct measurements of the mesospheric wind and temperature are obtained from the Doppler-shifted emission line at altitudes of 110 km on Venus and 75 km on Mars. (4) Detections of trace gases and isotopic ratios are performed without any ambiguity of the reproducing the terrestrial atmospheric absorptions in the observed wavelength range. A HDO measurement of twice the *Vienna Standard Mean Ocean Water* (VSMOW) can be obtained by 15-min integration, while H_2O of 75 ppm is provided by 3.62-h integration. The detectability of the 100 ppb-CH_4 on Mars corresponds to an integration time of 32 h.

1. General introduction

Recent successful explorations of planetary atmospheres by numerous spacecraft and ground-based telescopes have revealed their highly variable phenomena with spatial variations at various time scales such as diurnal, seasonal, and following the 11-year solar cycle. The characteristics of such spatial and temporal variations are essential for studying the atmospheric dynamics and photochemistry, and for understanding the meteorology, climatology, and the atmospheric evolution. However, many ground-based telescopes, particularly those with large apertures, are operated on a public time-sharing basis; therefore, they are not practical for conducting dedicated, continuous monitoring observations of planetary atmospheres. Spacecraft missions can be used for such observation; however, their spatial coverage is often strongly limited by the instantaneous field-of-view (FOV) of the instrument and the orbit of the spacecraft. Moreover, the monitoring capability is still limited to the mission lifetime. Complementary ground-based observations can probe regions that are not accessible remotely by spacecraft and can obtain global maps

* Corresponding author.
E-mail addresses: rom@pat.gp.tohoku.ac.jp (H. Nakagawa), shohei.aoki@iaps.inaf.it (S. Aoki), sagawa@cc.kyoto-su.ac.jp (H. Sagawa), kasaba@pat.gp.tohoku.ac.jp (Y. Kasaba), murata@pat.gp.tohoku.ac.jp (I. Murata), sonnabend@radiometer-physics.de (G. Sonnabend), sornig@ph1.uni-koeln.de (M. Sornig), okano@pparc.gp.tohoku.ac.jp (S. Okano), kuhn@IfA.Hawaii.Edu (J.R. Kuhn), ritter@IfA.Hawaii.Edu (J.M. Ritter), kagi@pparc.gp.tohoku.ac.jp (M. Kagitani), tsakanoi@pparc.gp.tohoku.ac.jp (T. Sakanoi), taguchi@rikkyo.ac.jp (M. Taguchi), takami@pat.gp.tohoku.ac.jp (K. Takami).

http://dx.doi.org/10.1016/j.pss.2016.04.002
0032-0633/

across the planetary disk. Continuous observation by a dedicated telescope for planetary science will be helpful for understanding the variable nature and spatial variations of planetary atmospheres.

We relocated our Tohoku 60 cm telescope (T60) from Fukushima, Japan, to the summit of Mt. Haleakalā, Hawaii, in September 2014. This telescope is designed to achieve continuous observations of planetary atmospheres through remote operation. In addition, we are currently conducting the Polarized Light from Atmospheres of Nearby Extra-Terrestrial System (PLANETS) project, in which a new 1.8 m telescope will be installed at the summit of Mt. Haleakalā for planetary science, including analysis of exoplanets, under an international consortium (http://kopiko.ifa.hawaii.edu/planets/index.html), see Sakanoi et al. (2014). The Mid-Infrared Laser Heterodyne Instrument (MILAHI) has been developed as a facility instrument for these planetary science-dedicated telescopes at the summit of Mt. Haleakalā, which is well suited for infrared (IR) spectroscopy at an altitude of 3055 m owing to low humidity and low atmospheric absorptions.

A number of rotational and vibrational transitions of atmospheric molecules in the mid-IR wavelength enable observation of many of the most important species and their isotopes in planetary atmospheres. IR heterodyne spectroscopy provides the highest spectral resolution at 7–12 μm with resolving power $R=\lambda/\Delta\lambda > 10^6$ and sensitivity close to the quantum limit. These features enable us to fully resolve the line shape of molecular transitions, which provides unique information of the atmosphere: (i) It allows to obtain vertical profiles of dynamics and thermal structure retrieved from single molecular line. (ii) It permits the study of local winds and temperature in the planetary upper atmosphere by using direct measurements of non-local thermodynamic equilibrium (LTE) emission. (iii) High-resolution spectroscopy is suitable for directly observing minor constituents in the planetary atmospheres without any ambiguity for reproducing the terrestrial atmospheric features. Notable successes on Venus, Mars, Jupiter, Titan, and Earth have been accomplished by *National Aeronautics and Space Administration* (NASA) Goddard Space Flight Center (GSFC; Kostuik and Mumma, 1983; Livengood et al., 1993; Kostuik, 1994; Kostuik et al., 1996; Fast et al., 2002), the University of Cologne (Sonnabend et al., 2010; Sornig et al., 2013), and Tohoku University (Okano et al., 1989; Fukunishi et al., 1990; Taguchi et al., 1990).

The present study proposes continuous observation of the atmospheric dynamics, thermal structure, and compositions on Mars and Venus and investigation of the nature of atmospheric activity on various time scales. In Section 2, we describe the IR heterodyne spectrometer technique and instrumentation. Next, we discuss the scientific objectives on Mars and Venus, which are focused on the benefit of high-resolution spectroscopy in Section 3. In Section 4, we address the scientific capabilities and measurement sensitivities by using modeling and predictions from the radiative transfer code. Finally, we summarize our conclusions in Section 5.

2. Instrument

2.1. Principle

The IR heterodyne detection is analogous to a spectroscopy technique in the radio frequency range. An IR source from the planet is combined with a laser local oscillator (LO) and is focused onto a mercury cadmium telluride (MCT) photodiode mixer. The resultant intermediate frequency (IF) in the radio region preserves the intensity and spectral information of the IR spectrum. Heterodyne detection is a coherent technique, and the detected electric field is the sum of the electric fields of the source and LO, $E(t)$:

$$E(t) = E_S \exp(i\omega_S t) + E_{LO} \exp(i\omega_{LO} t), \quad (1)$$

where radiation from the source (frequency ω_s, electric field $E_S\exp(i\omega_S t)$), and the output of an LO (frequency ω_{LO} , electric field $E_{LO}\exp(i\omega_{LO}t)$). The nonlinear response of the photodiode mixer is

$$R(t) \propto EE^* = E_S^2 + E_{LO}^2 + 2|E_S E_{LO}|\cos[(\omega_S - \omega_{LO})t], \quad (2)$$

where $\omega_s - \omega_{LO}$ is a cross-product term generated at IF.

Table 1
Instrumental specifications.

Size	W600 × D1200 × H450 mm for optics
Weight	80 kg
Wavelength	7–12 μm
Operating spectral range	7.71–7.73 μm (1293–1297 cm^{-1}) 9.54–9.59 μm (1043–1048 cm^{-1}) 10.28–10.33 μm (968–973 cm^{-1})
Detector	Mercury–Cadmium–Telluride photo diode
Detector elements	0.1 mm diameter
Detector bandwidth	3000 MHz (~0.10 cm^{-1}) (3 dB cut off)
Backend spectrometer	Digital Fast Fourier Transform spectrometer
Backend bandpass	1000 MHz (~0.03 cm^{-1})
Backend resolution	61 kHz (1.8×10^{-6} cm^{-1}) or 16,384 channels
Noise level	System noise temperature 3000 K
Resolving power	more than 1.5×10^6
Diffraction-limited FOV	4.32″ with 60 cm-telescope (10.3 μm) 1.44″ with 1.8 m-telescope (10.3 μm)
Focal plane operation	Coude or Nasmyth mounted

2.2. Specifications

The instrumental specifications of MILAHI are summarized in Table 1, and its optical configuration is shown in Figs. 1 and 2. MILAHI is currently composed of three LOs that cover the wavelength ranges of 7.71–7.73 μm (1293–1297 cm^{-1}), 9.54–9.59 μm (1043–1048 cm^{-1}), and 10.28–10.33 μm (968–973 cm^{-1}) and of one backend spectrometer. Previous systems have used large-sized CO_2 lasers, which allow observations in only a small portion of 9–12 μm. In contrast, recent applications of the quantum cascade laser (QCL) to the IR laser heterodyne have opened new spectral regions to exploration in 7–13 μm (Sonnabend et al., 2005; Stupar et al., 2008; Stangier et al., 2013). Because the current LOs in the system are easily exchangeable, observable molecules can be extended by handling with additional LOs. In our system, a newly designed room-temperature-type QCL manufactured by Hamamatsu Photonics is adopted for use as a LO. Temperature sweeping between −30 °C and 30 °C strongly increases the total tuning range, which is five times larger than the liquid nitrogen type QCL at 5 cm^{-1} for each wavelength region. Fig. 3 shows an example of the emission spectra of LO obtained using Fourier Transfer Spectrometer (FTS) with 0.0035 cm^{-1} resolution without any apodization. Due to the discontinuity of the interferogram-edge, the oscillation occurred around the peak line, which caused negative excursions and brunch of low-level features. The typical output power of LO is of 30–100 mW. We also applied a compact CO_2 gas laser manufactured by Access Laser Co. as a LO in MILAHI for complementary use in 10 μm. The CO_2 gas laser covers wavelength ranges of 9.20–9.34 μm (1071–1087 cm^{-1}), 9.45–9.69 μm (1032–1058 cm^{-1}), 10.15–10.34 μm (967–985 cm^{-1}), and 10.47–10.71 μm (934–955 cm^{-1}).

The optical beam from the celestial signal is combined with the LO on the ZnSe beam splitter and is fed into the MCT photodiode mixer, manufactured by Raytheon vision systems. We used four detector elements on a chip in the form of a 2 × 2 matrix. Each individual detector is circular with a diameter of 0.1 mm and 0.1 mm edge-to-edge spacing between each element. Each

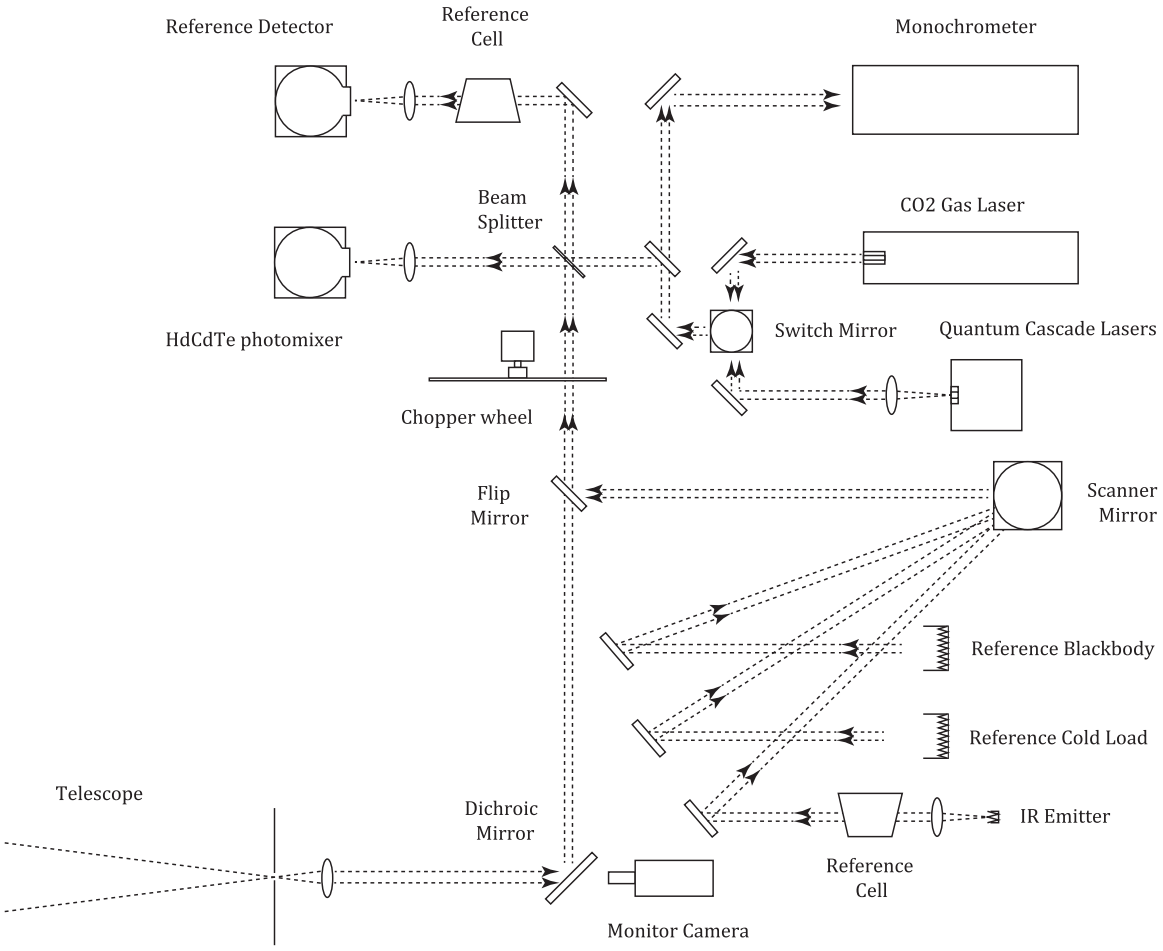

Fig. 1. Optical configuration of Mid-Infrared Laser Heterodyne Instrument (MILAHI).

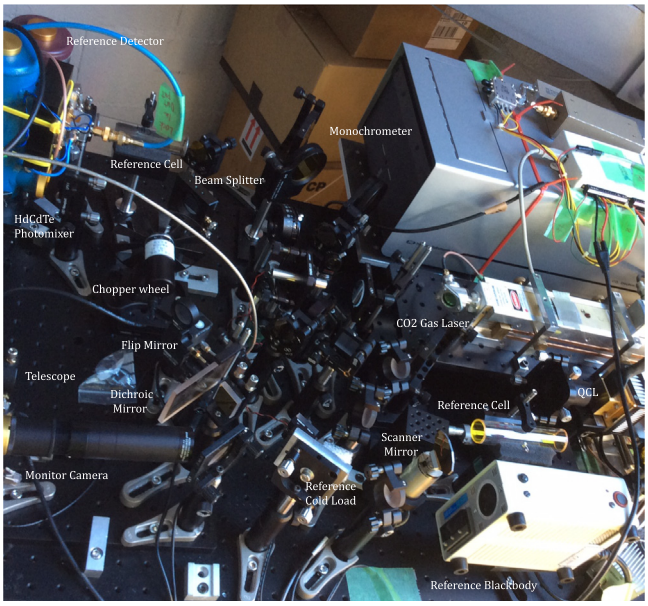

Fig. 2. View of the optics of Mid-Infrared Laser Heterodyne Instrument (MILAHI). The size of the shown optics is 600 mm in width, 1200 mm in depth, and 450 mm in height.

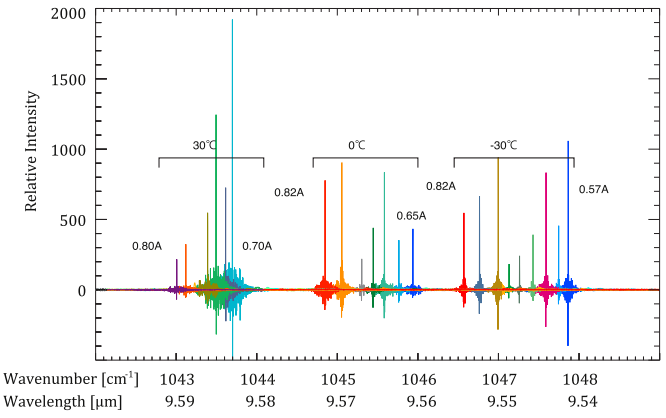

Fig. 3. Emission spectra of 9.6 μm quantum cascade laser (QCL) measured by Fourier Transform Spectrometer (FTS) with a spectral resolution of 0.0035 cm^{-1} without any apodization. Each single-mode emission spectrum was obtained by a certain temperature (−30 °C, 0 °C, +30 °C) and current of LO (600–950 mA, shown as colored lines with labeled). Intensity is given in arbitrary units. The typical output power of LO is of 30–100 mW. (For interpretation of the references to color in this figure legend, the reader is referred to the web version of this article).

detector optimizes the sensitivity at a specific wavelength to cover the wavelength range from 7–12 μm. The four elements were tuned to wavelength value of 8.3, 9.0, 9.6, and 10.3 μm. Each detector element was wired to an SMA output terminal, and selected outside the dewar. The photodiode mixer generates an IF signal with a bandwidth of 3 GHz in both the upper and lower sideband, which is known as double sideband detection. The mixer is cooled to the Liquid Nitrogen (LN_2) temperature in a dewar vessel which should be replaced by cryocoolers for continuous operation.

As the backend spectrometer, a Digital Fast Fourier Transform spectrometer (DFT) is first adapted to the IR heterodyne system based on a commercially available fast digital sampler with an on-board Field Programmable Gate Array (FPGA; Benz et al., 2008). Our DFT enables instantaneous coverage of 1 GHz, or 500 MHz in the high-resolution mode, resolved into 16,384 channels at 61 kHz corresponding to 0.000002 cm^{-1}, or 31 kHz in the high-resolution mode. To analyze a range of 0–1 GHz at IF, a signal is sampled every 0.5 ns. The theoretical limit of an 8-bit analog-to-digital converter (A/D) yields a dynamic range of 48 dB. DFT offers flexibility, well-controlled stability, inherent frequency calibration and linearity, and compactness compared with previously used spectrometers such as RF filter bank or an acousto–optical (AOS) spectrometer. The calibration subsystem consists of a calibrated black body, an absorber at ambient temperature, a reference gas cell, and a Galvano scanner mirror which can direct the planet, the sky, and the calibration targets. An offset position is optimized for each target. The calibrated spectrum is calculated by

$$J = \frac{S-R}{H-C}(J_H - J_C), \tag{3}$$

where S, R, H, and C denote the photon current from the signal (the planet), reference (the sky), hot load, and ambient temperature load, respectively, in a given time interval. The background are removed by taking the difference between S and R. Non-uniform gain of the receiver across the IF band is corrected by dividing by the calibration load differences between H and C. J_H and J_C (K) denote the brightness temperature of calibrators using known physical temperature, hot load (400 °C) and cold load (room temperature). Since we operate outside the range of the Rayleigh–Jeans approximation the brightness temperatures of the two loads at the operating wavelength are determined by Planck's law from the physical parameters T_{phy} and the quantum limit T_{ql} using

$$J = T_{ql}\left(\exp\left(\frac{T_{ql}}{T_{phy}} - 1\right)\right)^{-1}. \tag{4}$$

The factor $(J_H - J_C)$ enables us to perform absolute calibration by using the known temperatures of the calibration loads. Thus, Eq. (3) directly determines the brightness temperature difference between the signal and reference position, as shown by the detector, including all losses (Sonnabend et al., 2008).

2.3. Spectral resolution

The frequency stability of the LO and its line width determine the spectral resolution; thus, the optimum stabilization of the LO frequency is required. A compact thermo–electric air cooler head stabilizes the operating temperature of the LO with 0.1 °C precision. A typical example of observed spectra of the terrestrial ozone absorption at 1043.864 cm^{-1} is shown in Fig. 4. Spectra were observed by MILAHI using a 50 cm-coelostat at the University of Hawaii, Maui Advanced Technology Research Center (UH/ATRC) on March 11, 2014. The spectrum was obtained with 10-min integration for the background source, Sun, and the solar zenith angle was 30°. Data were resampled by 1 MHz-binning, and line positions were identified by using the high-resolution transmission (HITRAN) database (Rothman et al., 2013). The observed absorption spectrum strongly correlated with the synthetic spectrum including its isotope features. Fig. 5a shows the variation in the frequency position of the observed terrestrial ozone absorption. An extended view of the observed terrestrial ozone is shown in Fig. 5b. Data were taken every 6 s for 30 min. A Gaussian line profile was fitted to the terrestrial ozone absorption, yielding the line-center frequency. The observed peak-to-peak variation in the frequency was 30 MHz with a standard deviation of 20 MHz (0.0006 cm^{-1}), corresponding to the resolving power $R = 1.5 \times 10^6$.

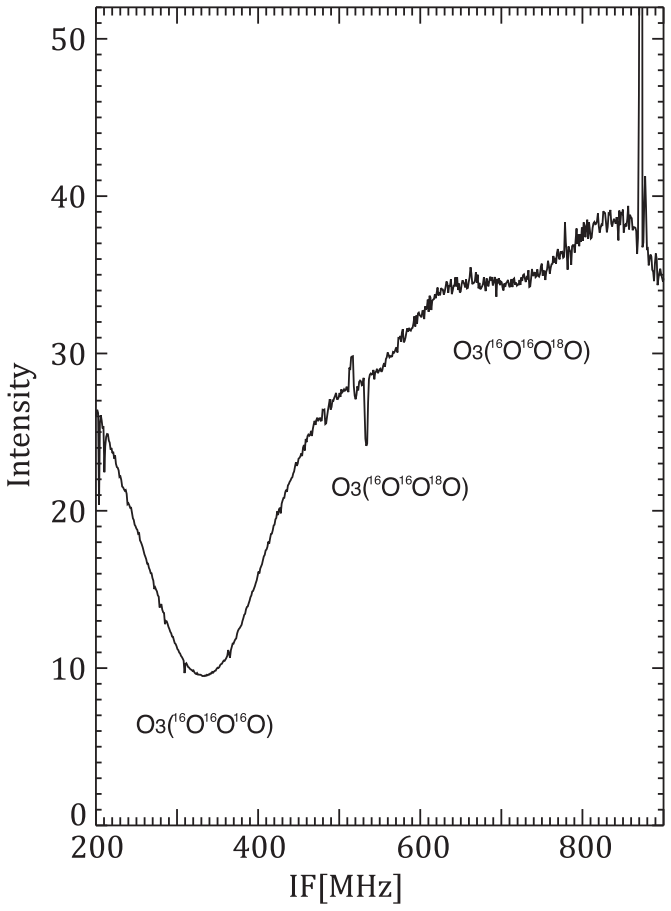

Fig. 4. Terrestrial ozone absorption spectrum at 1043.864 cm^{-1} (9.6 μm) obtained by by Mid-Infrared Laser Heterodyne Instrument (MILAHI). The spectrum was observed by using a 50 cm coelostat at the University of Hawaii, Maui Advanced Technology Research Center, in March 2014 with 10-min integration for the background target, Sun. The data were re-sampled with 1 MHz-binning. The unit of the intensity is *S-R*/*H-C* shown in the Eq. (3). The molecular line positions were identified by using the high-resolution transmission (HITRAN) database.

The absorption features of reference C_2H_4 and CH_4 gas cells with a pressure of 5 mbar was used for additional frequency-locked feedback to achieve a better frequency stability of 1 MHz ($R = 3.0 \times 10^7$; Sonnabend et al., 2008). In addition, the frequency drift can be easily corrected owing to the simultaneous detection of the reference gas cell during observation.

To measure the line width of the LO, we performed direct heterodyne measurement by using QCL as an input signal to our CO_2 laser-based heterodyne system. Fig. 6 shows the detailed features of the QCL emission line obtained at 1 s intervals. The result implies that the line width of our QCL is less than 20 MHz. Although the result satisfies our requirements for observing targets, it is noted that the line width of our QCL appears to be larger than 1 MHz, which is expected for LN_2-type QCL (Sonnabend et al., 2005).

Since the original backend-resolution of DFT, 61 kHz, is much finer than the frequency stabilization of LOs as mentioned above, the spectral resolution would be determined by the frequency stabilization of LOs. The fine channels of the backend are usually binned in order to reduce the spiky noise due to the surrounding radio noise source and DFT itself as well. The binning-width would be determined to balance both its scientific requirement (spectral resolution) and signal-to-noise ratio.

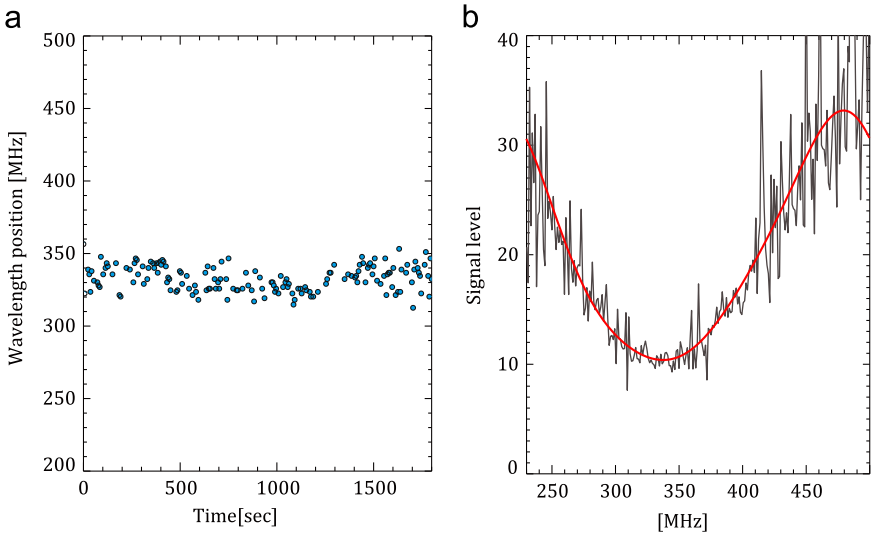

Fig. 5. Wavelength stability of the local oscillator (LO). (a) Variations in the fitted frequency position of the terrestrial ozone absorption line. Data were taken every 6 s over 30 min. The wavelength position is distributed in the range of $\pm$20 MHz, corresponding to $\pm$0.0006 cm^{-1}; 1 MHz corresponds to ~0.00003 cm^{-1} (b) Extended view of the observed terrestrial ozone absorption taken at 6 s intervals. A Gaussian line profile (red line) was fitted to the terrestrial ozone absorption, yielding the line-center frequency. The unit of the intensity is *S-R/H-C* shown in the Eq. (3). (For interpretation of the references to color in this figure legend, the reader is referred to the web version of this article).

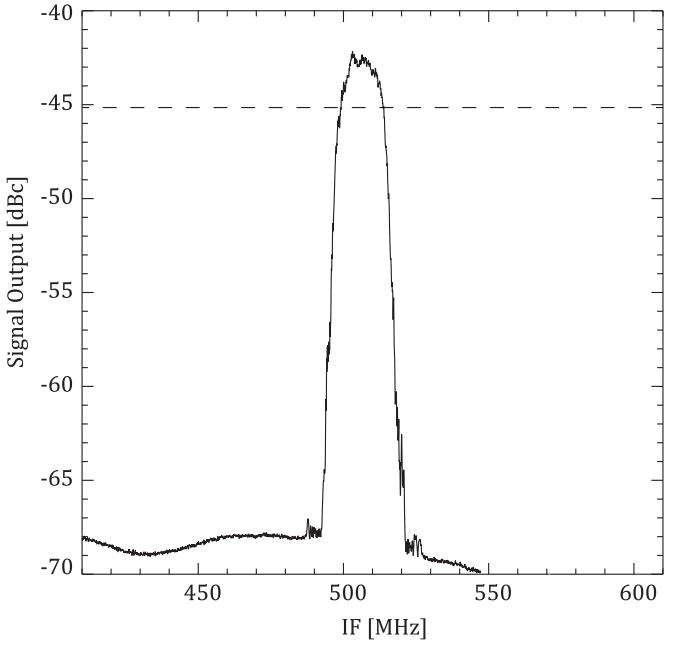

Fig. 6. Detailed feature of the quantum cascade laser (QCL) emission line obtained by direct heterodyne measurement with a CO_2 laser-based heterodyne system at 10.3 μm at 1 s intervals. The full width at half maximum (FWHM) of the line width is less than 20 MHz (0.0006 cm^{-1}), as shown as the dotted line.

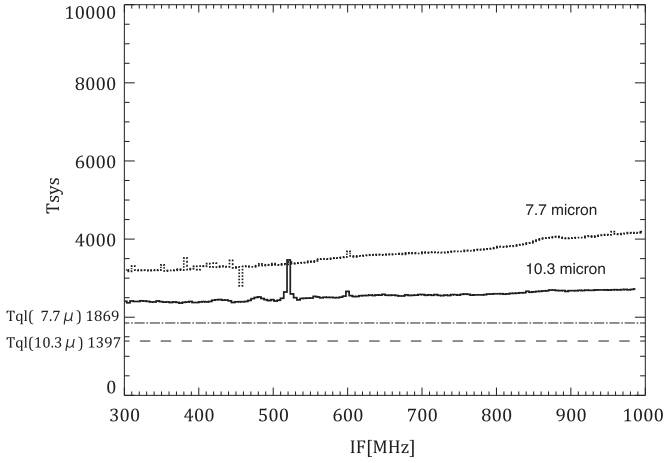

Fig. 7. System noise temperature T_{sys} at 10.3 μm (solid) and 7.7 μm (dotted). The averaged value of 2500 K of T_{sys} at 10.3 μm is less than a factor of two above the quantum limit T_{ql}. The spectral binning is 4 MHz. It is noted that T_{ql} equals 1397 K at 10.3 μm and 1869 K at 7.7 μm.

2.4. Sensitivity

Fig. 7 shows the typical sensitivity over the full 1 GHz bandwidth of the DFT. The averaged system noise temperature T_{sys} reached 2500 K at 10.3 μm, and 3500 K at 7.7 μm. Neglecting all additional noise sources, a heterodyne system has a natural limit known as quantum limit T_{ql} which is the minimum noise contribution of a classical mixer in an ideal system that limits the sensitivity of any heterodyne receiver:

$$T_{ql} = \frac{h \cdot \nu}{k_B}, \tag{5}$$

where k_B is the Boltzmann constant, h is the Planck constant, and ν is the observed frequency. T_{ql} equals 1397 K at 10.3 μm and 1869 K at 7.7 μm. The system noise temperature 2500 K obtained by MILAHI at 10.3 μm is only 70% above the quantum limit. This corresponds to a minimal detectable brightness temperature difference:

$$\Delta T = \frac{T_{sys}}{\sqrt{B_{res} \cdot t_{int}}}, \tag{6}$$

where B_{res} is the spectral resolution bandwidth 1.5 MHz, and t_{int} the integration time 10 min for 50 mK (0.4 ergs/s cm^2 cm^{-1} sr) in a minimum flux difference for extended sources (Sonnabend et al., 2008). In addition, the characteristics of the bandwidth in Fig. 7 are flat and clean with no standing waves in the IF processing electronics.

2.5. Observation conditions at Haleakalā

A summary of the beam size (instrumental FOV) with a diffraction limited etendue $A_D\Omega$, where A_D is the effective aperture

Table 2
Beam size of the instrument and the apparent sizes of the planets.

LO	Spectral bands (cm^{-1})	Beam size (60 cm)	Beam size (1.8 m)
1	968–973	4.32″	1.44″
2	1043–1048	4.03″	1.34″
3	1293–1297	3.23″	1.08″

c.f. Apparent size of Venus ~10–60″, Mars ~3–25″.

and Ω is the beam solid angle, depending on the wavelength λ, is shown in Table 2. In contrast to existing single-dish millimeter–submillimeter observations, MILAHI offers a significantly higher spatial resolution, allowing detailed studies of variations with latitude and local time across the planetary disk. This instrument will provide 4.2 arcsec resolution with the T60 telescope and 1.4 arcsec resolution with the 1.8 m telescope at 10.3 μm. For example, the angular diameter of the apparent disk of Venus varied from 10 arcsesc to 58 arcsec. In contrast, that of Mars varied from 3 arcsec to 25 arcsec. It is remarkable that T60 still has significantly better spatial resolution than a larger submillimeter telescope such as the JCMT 15 m diameter telescope with a diffraction limited beam size of 14 arcsec. The PLANETS 1.8 m telescope can achieve spatial resolutions of about 400 km on Mars and 200 km on Venus at their maximum angular diameters. In contrast, a limitation of IR heterodyne technique, comparing with long-slit mapping spectrometers, is that different FOVs are registered sequentially and not simultaneously. Mapping requires the adequate time, which depends on the number of positions and the integration time for each position. Note that the seasonal and annual variations of maps can be investigated by weekly/monthly survey. For fast-changing phenomena, FOV should be fixed in the specific location on planetary disk.

To ensure accurate orientation on the target source, a dichroic mirror splits the emissions from the target and reflects the IR emission. In contrast, visible emission is transmitted into an optical guide system. The full FOV of the guide camera is about 100×100 arcsec. The detected image of the *Complementary Metal Oxide Semiconductor* (*CMOS*) camera can be used for feedback to stabilize the orientation.

Bradley et al. (2006) reported information on the summit conditions of observation at Haleakalā. The averaged cloud-free line of sight percentage in the nighttime (daytime) was about 70% (62%). When we simply assume 70% in total operation (12 h per night) and time-sharing with three facility instruments onboard T60, about 1022 h per year are provided for MILAHI operations. Since the MILAHI can also operate during the daytime without any competitions with other instruments, the operation time basically increases more. Such a huge amount of observation time enables the investigation of physical parameters for various time-scales including the 11-year solar cycle and detection of minor constituents with long-term integration. The operation will be utilized under remote control to achieve continuous measurement of the planetary atmospheres.

3. Scientific objectives on Mars and Venus by high-resolution spectroscopy

3.1. Temperature profiles in the upper atmosphere on Venus

Spectrally resolved molecular line shapes enables us to retrieve vertical profile of atmospheric temperature and molecular abundance by taking information from pressure-broadened line widths. In addition, the IR technique is highly sensitive to detection of narrow nearly Doppler-broadened features, which would reach the upper atmosphere. Millimeter and submillimeter observations of CO rotational lines have been used to retrieve the temperature profile over the ~80–115 km altitude region on Venus (e.g., Lellouch et al., 1994; Clancy et al., 2012). These studies illustrate the presence of strong diurnal and spatial variabilities, which are still poorly understood. Stangier et al. (2015) demonstrated the temperature sensitivity of IR heterodyne spectroscopy between 60–90 km, based on the observed nightside spectra of Venus. Since IR heterodyne spectroscopy offers a higher spatial resolution compared to those millimeter and submillimeter observations, measurements with IR heterodyne spectroscopy across the global disk will improve our understanding of the variability to distinguish temporal and spatial variations. From spaceborne measurements, the Venus Express (VEX) mission addressed in detail the upper atmosphere on Venus by using the Spectroscopy for Investigation of Characteristics of the Atmosphere of Venus/Solar Occultation at Infrared (SPICAV/SOIR) instrument (e.g., Bertaux et al., 2007; Mahieux et al., 2012) and Radio Science experiment (VeRa) (e.g., Pätzold et al., 2007; Tellman et al., 2009). However, VEX no longer exists so that there is no immediate prospect for new measurements to characterize the Venus upper atmosphere. Instead, the Japanese Akatsuki spacecraft has entered orbit around Venus on December 2015. The cameras in the wavelength range from ultraviolet to IR onboard spacecraft study different atmospheric features in and beneath the cloud layer. Ground-based measurement of IR heterodyne spectroscopy will extend and complement the Akatsuki data into the upper atmosphere.

3.2. Temperature profiles in the lower atmosphere on Mars

Regarding the Martian atmosphere, abundant data observed by the Thermal Emission Spectrometer (TES) onboard the Mars Global Surveyor (MGS) are available for the thermal structure in the lower atmosphere, up to 40–50 km, including horizontal distributions and seasonal changes through several Martian years (Smith, 2001). A global map of thermal structure is one of the key but missing parameters needed for studying unique climate events on Mars such as a dust storm. Atmospheric dust is a striking characteristic of the Martian environment, and dust storms are very frequently observed. Those at the planet-encircling scale are known as global dust storms, which are maintained for months and lift a large amount of dust into the atmosphere. These floating dust particles block sunlight from reaching the surface and absorb solar radiation, which directly heats the atmosphere (Smith et al., 2002). Such a dramatic change in the thermal structure induces significant modulation in the dynamics and the compositions as well in a global scale. However, a full disk map of the thermal structure during a dust storm event is not well understood. Ground-based telescopes are unique tools used to measure such a global map of thermal structure. Thus far, single-dish millimeter observations of CO have been performed to obtain temperatures of 0–70 km and wind speed near 50 km in altitude (Clancy et al., 1990). Such observations, however, lack spatial resolution owing to the large FOV of the telescope at such wavelengths and are incapable of resolving the Martian disk. A few millimeter interferometry measurements have resolved this problem (Moreno et al., 2009), although the synthesized beam, about 0.5×0.25 times smaller than the Martian angular diameter, is still insufficient for explaining the physical processes behind the observed thermal and wind structures. For instance, several 100-km resolution maps could be helpful to understand the evolution of dust storm and its effect on the background fields. The MILAHI observation will allow us to monitor the thermal structure global map.

3.3. Wind profiles in the upper atmosphere on Venus

Ultra-high-resolution spectroscopy can provide wind velocity retrievals in the upper atmosphere on Venus. Thus far, sub-millimeter observations have allowed direct measurement of the wind velocity projected to the line-of-sight direction by measuring the Doppler shift of molecular lines. This method is sensitive to wind at altitudes of 95–110 km (e.g., Clancy et al., 2012). The distributions of NO and O_2 nightglow are also used to indicate wind velocities at altitudes of 95–115 km (Hueso et al., 2008). Visible spectroscopy from ground-based measurement has also established winds near 68 km (around the cloud top layer) from the Doppler shift of solar radiation reflected by clouds (e.g., Widemann et al., 2007). In addition, a cloud tracking method from successive images can determine wind velocities in the cloud top layer at 60 km (Peralta et al., 2012; Kouyama et al., 2012). However, this method cannot be applied for other altitudes in the mesosphere in which no tracing features are available. New direct wind measurement of the missing layer between 70 km and 90 km by IR heterodyne spectroscopy will comprehensively enhance our understanding of the manner on which the retrograde zonal flow at the cloud layer couples with subsolar-to-antisolar flow in the thermosphere.

3.4. Wind profiles in the lower atmosphere on Mars

Wind measurements in the Martian lower atmosphere are still limited. Single-dish millimeter observations of CO have provided us with the first wind measurements near the altitude of 50 km (e.g., Clancy et al., 2006). Moreno et al. (2009) mapped the retrieved wind velocities near 50 km by using the Institut de Radioastronomie Millimétrique (IRAM) Plateau de Bure Interferometer. Although they reported strong variabilities of mesospheric zonal wind in the range of 70–170 m/s, the models do not show such spatial structure and diurnal variations. A new direct wind measurement from near-surface to the lower atmosphere by IR heterodyne spectroscopy will restrict the global circulation related to dust activity and water cycle. It will also reveal the generation and propagation of small-scale gravity waves (GW) caused by mountainous regions and the meandering winter polar jet (Kuroda et al., 2015).

3.5. Direct measurements of wind and temperatures in the middle atmosphere

Direct measurements of wind and temperature can be accomplished with CO_2 non-LTE emission line measurements (e.g., Betz et al., 1976; Deming et al., 1983; Goldstein et al., 1991; Sornig et al., 2008; Sonnabend et al., 2010). The predicted narrow altitude range of this emission enables estimation of the wind velocity at altitudes of approximately 110 ± 10 km on Venus and 75 ± 10 km on Mars (López-Valverde et al., 2011). The local wind velocity and temperature can be determined without using radiative transfer model calculations. IR heterodyne spectroscopy is highly sensitive to detecting such narrow Doppler features. Fig. 8 shows a typical example of the Venusian atmospheric CO_2 non-LTE emission spectrum observed by single measurement of MILAHI with T60 on September 2nd, 2015, with a total integration time of 40 min. About 44% of the total integration time is spent on the source, Venus. For the tunable QCLs, we used the absorption line of C_2H_4 as a reference frequency to determine the LO frequency. The rest frequency of the targeted line was shifted to correspond to the known topocentric radial velocities between Earth and Venus in addition to the Doppler shift owing to the atmospheric wind on Venus.

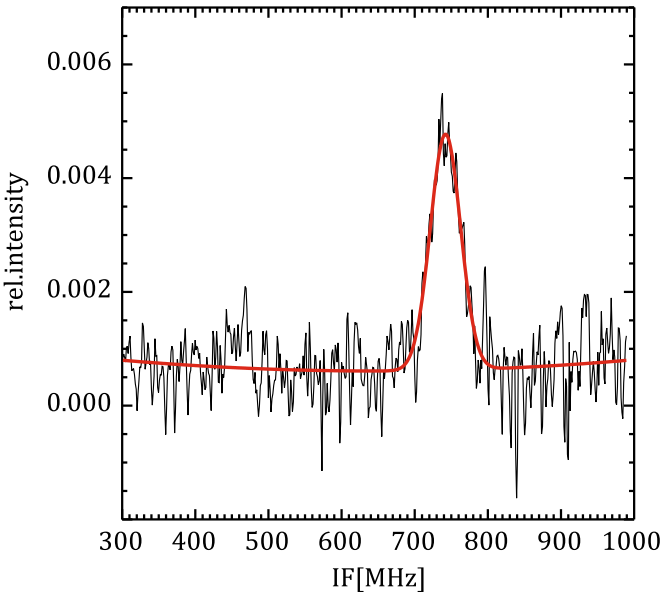

Fig. 8. Example of the Venusian CO_2 non-LTE emission spectrum at 10.5 μm obtained on September 2nd, 2015, by single measurement with a total integration time of 40 min by Mid-Infrared Laser Heterodyne Instrument (MILAHI) on the Tohoku 60 cm telescope (T60). The red line shows the Gaussian curve fit to the data. The unit of the intensity is *S-R*/*H-C* shown in the Eq. (3). (For interpretation of the references to color in this figure legend, the reader is referred to the web version of this article).

On Venus, many atmospheric wave features in the cloud layer (Markiwicz et al., 2007; Peralta et al., 2008, Titov et al., 2012) potentially play a major role for atmospheric coupling through the effects of momentum transport and eddy mixing. The VeRa onboard VEX obtained temperature profiles covering an altitude range of 40–90 km (Tellman et al., 2013) and revealed many small-scale wave structures possibly caused by gravity waves above the cloud layer over a wide range of spatial scales and local times. Nakagawa et al. (2013) implied that such small-scale gravity waves could cause strong wind perturbations in the lower thermosphere. Long-term monitoring of the lower thermosphere wind oscillations will clarify the characteristics of upward propagating gravity waves and their breaking.

In the case of the middle atmosphere on Mars, the Mars Climate Sounder (MCS) onboard the Mars Reconnaissance Orbiter (MRO) has greatly extended our knowledge of the 70–80 km altitude range by using limb-geometry observations (McCleese et al., 2008) to reveal strong variabilities in the middle atmosphere owing to tidal and gravity waves. In particular, gravity waves are important in defining large-scale winds and eddy diffusion in the mesosphere and thermosphere. Medvedev et al. (2011) discussed the manner in which large-scale winds are modified by drag owing to gravity wave from the lower atmosphere. In contrast, gravity waves in the Martian thermosphere are highly variable in space and time (Creasey et al., 2006; Fritts et al., 2006). To determine the variability of gravity waves and investigate their effects on the vertical transport of atmospheric composition and its momentum energy, temperature and wind in the transition layer, the mesosphere, should be investigated under the different atmospheric conditions in the lower atmosphere. Further investigations of the three-dimensional thermal structure and wind velocity for local time, latitude, longitude, and solar longitude (Ls) should also lead to improvement in our ability to simulate the Martian climate system.

3.6. Methane on Mars

The detection of CH_4 in the Martian atmosphere as a signature of biological/geological activities continues to be debated (Krasnopolsky et al., 2004; Formisano et al., 2004; Encrenaz et al., 2005; Encrenaz, 2008; Mumma et al., 2009; Fonti and Marzo, 2010; Geminale et al., 2011; Zahnle et al., 2011; Krasnopolsky, 2012; Villanueva et al., 2013; Sonnabend et al., 2013; Webster et al., 2013). Encrenaz et al. (2005) using thermal imaging spectroscopy around 8 μm, derived for CH_4 an upper limit 20 ppb in the morning side and 70 ppb in the evening side. Mumma et al. (2009) reported that CH_4 concentrations appear to be locally enhanced at mixing ratios of up to 40 ppb in northern summer and change with the season; these results were not predicted by the current Mars global climate model (Lefèvre, and Forget, 2009). Geminale et al. (2011) suggested that CH_4 has increased over the north polar cap during northern summer. However, its reservoirs, release mechanisms, sinks, and circulation in the atmosphere remain unknown. In addition, the validity of these detections has been doubted by Zahnle et al. (2011). Due to the numerous other molecular features of the terrestrial atmosphere and Martian atmosphere in the same wavelength region, there is an ambiguity for reproducing the other spectral features surrounding the target line. The Tunable Laser Spectrometer (TLS) onboard the Curiosity rover has enabled sensitive detection of CH_4 (0–10 ppb) on Gale crater (Webster et al., 2014). However, a detection of CH_4 is valid only for the specific landing site of the rover. Sonnabend et al. (2013) reported the first attempt to search for CH_4 using by high-resolution IR heterodyne spectroscopy in the 7.8 μm wavelength region with resolving power and frequency precision of more than 10^6. However, a lack of observation time owing to bad weather conditions and a telluric opacity greater than anticipated has led to reduced signal-to-noise ratios; thus, no absorption was detected and upper limits of only 100 ppb were retrieved for the CH_4 concentration. Long-term operation of a dedicated telescope with such an ultra-high spectral resolution instrument will resolve this problem and contribute to understanding the potential seasonal/spatial variations of CH_4 across the Martian disk.

3.7. Water vapor isotopes HDO/H_2O on Mars

The *D*/*H* isotopic ratio present in the Martian atmosphere is a powerful tracer for understanding the atmospheric escape and water cycle by sublimation–condensation process (Yung et al., 1988; Owen et al., 1988; Montmessin et al., 2005; Novak et al., 2011; Villanueva et al., 2015; Aoki et al., 2015b). Villanueva et al. (2015) reported strong isotopic anomalies and seasonal variations of HDO/H_2O in the current Martian atmosphere by using high-spectral spectroscopy. They indicated a low HDO/H_2O of 1–3 with respect to (wrt) *Vienna Standard Mean Ocean Water* (VSMOW): HDO/$H_2O = 3.11 \times 10^4$ (Owen et al., 1988) at the winter hemisphere and very high HDO/H_2O of 9–10 wrt VSMOW at orographic depressions. A current general circulation model including the sublimation–condensation process (Montmessin et al., 2005) could not explain such strong anomalies; therefore, the existence of multiple ice reservoirs having different HDO/H_2O values is possible (Fisher, 2007). Usui et al. (2015) reported a low value of 2–3 wrt VSMOW for HDO/H_2O in quenched and impact glasses in Martian meteorites, which suggests the current existence of additional underground water/ice reservoirs on Mars. Mapping of HDO/H_2O with high accuracy enables identification of subsurface–atmosphere interaction and its reservoir.

Since the width of the Martian H_2O and HDO lines in the near-IR range is very narrow (0.01 cm^{-1}), an insufficient spectral resolution would cause large uncertainty for HDO/H_2O ratio. The best spectral resolution among existing near-IR spectrometers is 0.03 cm^{-1} at 3000 cm^{-1}. This value corresponds to $R = 10^5$ obtained by the cryogenic high-resolution infrared echelle spectrograph (CRIRES) onboard Very large telescope (VLT), which still cannot resolve the narrow Martian H_2O and HDO lines. Measurements of fully resolved molecular lines will be most appropriate for precise determination of such isotopic diagnostics.

In addition, the Mars Atmosphere and Volatile Evolution (MAVEN) spacecraft has been gathering information of *D*/*H* in the Martian upper atmosphere since its orbit insertion in September 2014 (Jakosky et al., 2015). By comparing the *D*/*H* in the upper atmosphere with HDO/H_2O in the lower atmosphere simultaneously, the vertical transport of water from the surface to space can be constrained. From this aspect, vertical information of HDO/H_2O is also urgently needed.

It is noted that measuring isotopes of carbon and oxygen in the carbon dioxide is also accessible by the current LOs of MILAHI, which will be addressed in the future works.

3.8. SO in the Venusian mesosphere

Several ground-based measurements in IR-submillimetre regime reported the SO_2 in the venusian atmosphere (Encrenaz et al., 2012, 2013; Sandor et al., 2010, 2012). The VEX mission results clarified long-term variations of the SO_2 mixing ratio in the Venusian atmosphere by comparison with the Pioneer Venus measurement in the 1980s (Marcq et al., 2013). Although the current LOs of MILAHI are not accessible for 8.0 μm for SO_2, MILAHI has the capability of extending its applications by handling additional LOs in the current framework. Thus, it is noted that the measurement of mesospheric SO_2 and its long-term monitoring would be an excellent science case for IR heterodyne spectroscopy in the future.

4. Scientific capabilities and measurement sensitivities

In this section, we address the scientific capabilities and measurement sensitivities for the targets as mentioned in the last section by numerically simulating the observations with the radiative transfer and inversion models. Table 3 shows a summary of the physical parameters with the expected sensitivities derived from this study.

Table 3
Summary of the sensitivity obtained in this study.

Physical parameter	Target	Alt. range [km]	Ver. res. [km]	Precision (assumed measurement noise, or integration time)
Temperature (retrieval)	Mars	0–30	10	4–10 K (1.0 [erg/s/cm^2/sr/cm^{-1}])
	Venus	65–90	5	3–12 K (1.0 [erg/s/cm^2/sr/cm^{-1}])
LOS wind (retrieval)	Mars	10–25	10	20–30 m/s (1.0 [erg/s/cm^2/sr/cm^{-1}])
	Venus	80	10	20 m/s (1.0 [erg/s/cm^2/sr/cm^{-1}])
LOS wind (mesosphere)	Mars	75	10	20 m/s
	Venus	110	10	$<$ 10 m/s
Temperature (mesosphere)	Mars	75	10	$<$ 10 K
	Venus	110	10	$<$ 10 K
H_2O	Mars	–	–	75 ppm (3.62 h)
HDO	Mars	–	–	96 ppb (2 SMOW) (15 min)
H_2O_2	Mars	–	–	10 ppb (1.3 h)
CH_4	Mars	–	–	10 ppb (32 h)

4.1. Simulation of observations

The measurement sensitivity of MILAHI was investigated by simulating the retrieval of the applicable physical parameters. We used the Advanced Model for Atmospheric Terahertz Radiation Analysis and Simulation (AMATERASU), which performs line-by-line radiative transfer and numerical modeling of instrumental characteristics and inversion calculations. A detailed description of this model can be found in Baron et al. (2008). To solve the ill-posed inversion problem, we used the least squares method with a priori constrains. It is noted that the a priori constraint (i.e., a priori error) employed here works as tuning parameters to change the weight between the covariance matrices of measurement and null-space errors. To synthesize the observation data (MILAHI measurement spectra), we calculated the forward model assuming a certain state vector of the applicable atmospheric physical parameters such as temperature profile and line-of-sight wind velocity, which we refer to as the "true state". Random noise is added on the calculated spectrum to obtain a synthetic measurement spectrum. The amplitude of random noise was set as 1.0 [erg/s/cm^2/sr/cm^{-1}] for 1 MHz spectral resolution, which is a typical value for an observation with a few hours of data integration. This synthesized measurement spectrum is used for inversion calculation, which yields as output the retrieved state vector. The a priori profile is set independent of the true state. The difference between the true and retrieved states gives the accuracy of the retrieval, and the $1-\sigma$ uncertainty of the retrieved state gives the precision of the retrieval. The sum of the accuracy and precision can be used to evaluate the quality of the retrieval. It is noted that the obtained retrieval quality depends on the true state used in the simulation. Therefore, the simulation was repeated 200 times for each science target by randomly selecting a different true state for each run. The mean of the quality of the retrieval from these 200 repetitions was finally regarded as the sensitivity of the measurements. By using this procedure, the vertical resolution of the measurement is also inferred by examining the averaging kernel matrix (a matrix describing the sensitivity of the retrieved state on the true state). More detail theoretical description about the retrieval methodology, including the derivation of the averaging kernel matrix, is found in Rodgers (2000).

4.2. Temperature profiles on Venus

The atmospheric temperature profile is retrieved from atmospheric spectra of optically thick lines. A single CO_2 absorption line is used to probe the thermal structure on Mars and Venus. We simulated the temperature retrieval from nadir geometry using CO_2 absorption line at R14 (971.930 cm^{-1}) for both Mars and Venus cases.

Fig. 9a shows the Venusian synthetic spectrum of a CO_2 absorption line with nadir geometry. In the case of Venus, the background radiation at this wavelength region originated from the cloud top. Here, we assumed the background temperature at the cloud tops to be 262.8 K at an altitude of 60 km based on the Venus reference atmosphere model VIRA (Seiff, 1985). We smoothed the spectrum to 10 MHz resolution; thus, the noise root–mean–square (RMS) error is reduced by a factor of the square root of 10. Fig. 9b shows an example of the retrieval simulation for Venus temperature profile using the synthetic measurement spectrum shown in Fig. 9a. The assumed true profile, a priori profile, and the retrieved profile with bars indicating the vertical resolution and retrieval error are shown. The $1-\sigma$ uncertainty of the retrieval (the mean of the retrieval accuracy over 200 tests of the retrieval simulation) are shown in Fig. 9c. Our results indicate that temperature retrieval can be obtained from altitudes of 65–90 km. The $1-\sigma$ uncertainty of the temperature retrieval is estimated to be 3–12 K, and a vertical resolution of 5 km is achieved. The sensitive altitude range complements the measurements by the submillimeter/millimeter regime at altitudes of 80–115 km, extending the vertical information of thermal structure above the cloud layer. In contrast, radio occultation measurements onboard spacecraft such as Venus Express, and Akatsuki address similar altitude regions of 40–90 km. Because their global coverage requires year-time integration, global mapping by IR heterodyne spectroscopy complements their limited spatial coverage and provides a three-dimensional structure of the mesospheric temperature.

4.3. Temperature profiles on Mars

Fig. 10a shows the Martian synthetic spectrum of the CO_2 absorption line from nadir geometry. Similar to that performed for Venus, we smoothed the spectrum into 10 MHz resolution in order

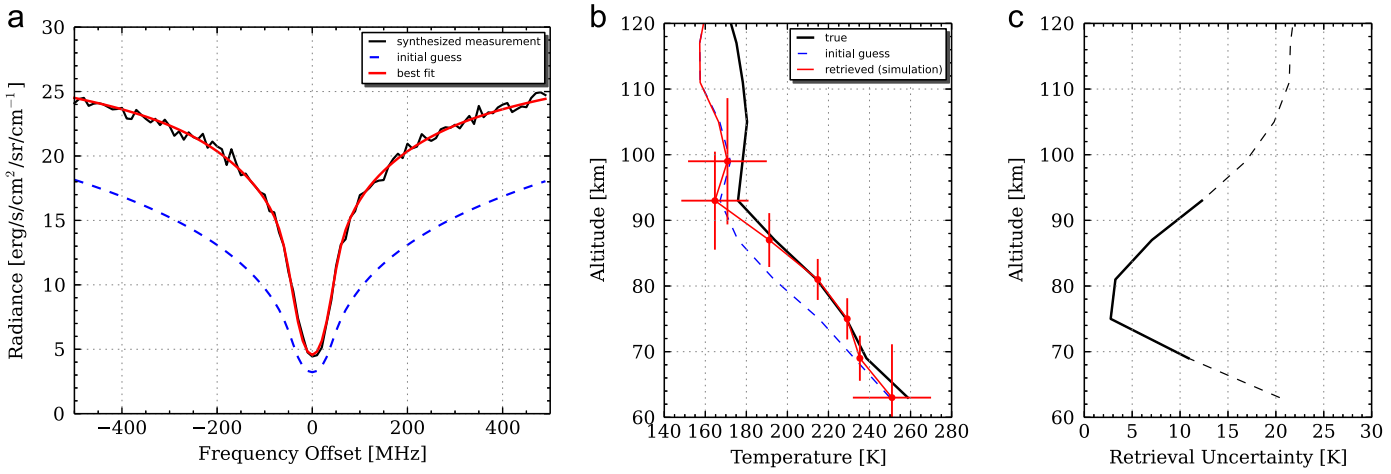

Fig. 9. Simulation of temperature profile retrieval on Venus. (a) Synthetic spectrum (black) of the CO_2 absorption line at R14 (971.930 cm^{-1}). The root–mean–square (RMS) noise is assumed to be 1.0 erg/s/cm^2/sr/cm^{-1}. The spectral binning-width is 10 MHz for the temperature retrievals. The red line represents the best-fit spectrum obtained with the retrieval simulation, while the blue denotes the spectrum obtained with the a priori temperature profile. Nadir geometry is assumed for simulations. (b) Example of the retrieved temperature profile (red line), a-priori profile (blue line), and the assumed true profile (black). $1-\sigma$ precision of the retrieval error is shown with a horizontal bar, while the vertical resolution is shown with a vertical bar. (c) Expected uncertainty of temperature retrieval. See the text for the detail explanation. The sensitive region is shown as a solid line. (For interpretation of the references to color in this figure legend, the reader is referred to the web version of this article).

to increase signal-to-noise ratio. Fig. 10b shows the retrieval simulation for the Martian temperature profile from the synthetic spectrum for Mars shown in Fig. 10a. The $1-\sigma$ retrieval uncertainty is shown in Fig. 10c. Temperature retrieval can be obtained from the surface to an altitude of 30 km; the $1-\sigma$ uncertainty of temperature retrieval is estimated to be 4–10 K. A vertical resolution of ~10 km is achieved. By investigating the sensitivity at the equator for various Martian seasons (L_s), our simulations showed that temperature sensitivity could be reached for 40 km altitude during warm temperature conditions (not shown). IR heterodyne spectroscopy has the sensitivity for probing the lower atmospheric region, which is comparable to existing IR spaceborne observation. IR heterodyne with ground-based telescopes complements the global-map measurement of the thermal structure at the lower atmosphere. Regarding the altitude range of the measurement response for both Venus and Mars, the upper limit of the temperature retrieval was determined to be around the 0.1 hPa pressure level, corresponding to altitudes of 90 km for Venus and 40 km for Mars. Our sensitivity estimation shows good agreement with the previous study (Stangier et al, 2015).

4.4. Wind profiles on Venus

We propose new retrievals of winds by using IR heterodyne spectroscopy. The predominant wind velocity as well as temperature at different altitude layers can be also deduced from a CO_2 absorption line. For wind retrievals, we smoothed the spectrum into 1 MHz resolution.

Fig. 11a shows the synthetic spectrum of CO_2 absorption at R14 (971.930 cm^{-1}) from limb geometry on Venus. As shown in Fig. 11b, the measurement has a sensitivity to wind at the altitudes of 80 km with 10 km vertical resolution. The expected uncertainty of the wind retrieval is limited as ~20 m/s as seen in Fig. 11c due to the relatively low signal-to-noise of the measurement. Despite of the limited sensitivity, our simulation indicates that IR heterodyne spectroscopy measurements open the sensitivity at an

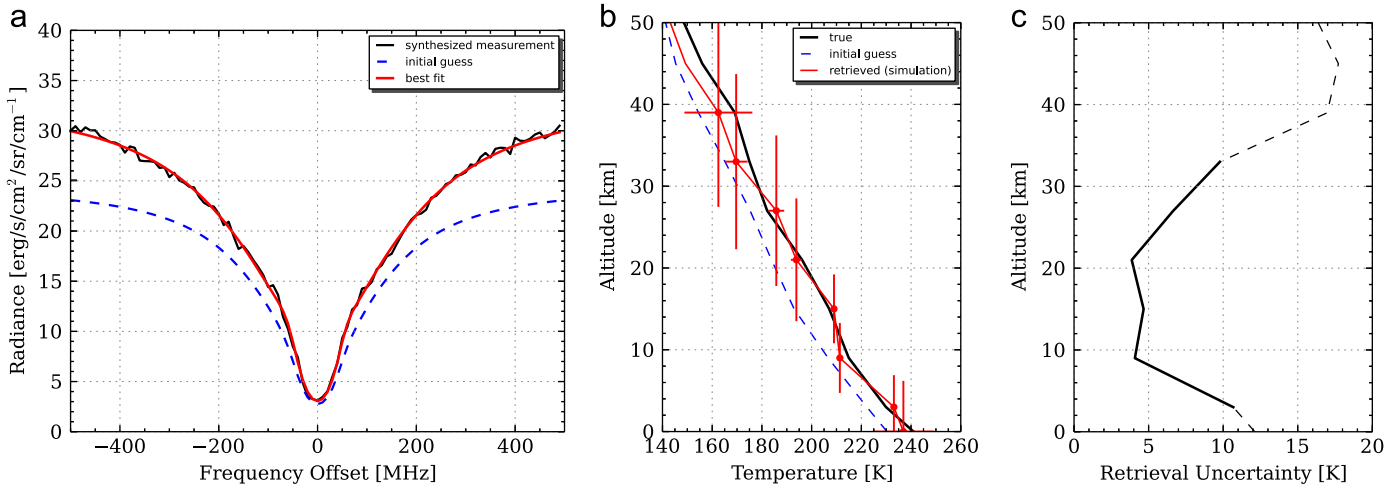

Fig. 10. Simulation of the temperature profile retrieval on Mars. The figure format is as same as that for Fig. 9. (a) Synthetic spectrum (black) of the CO_2 absorption line at R14 (971.930 cm^{-1}). The root–mean–square (RMS) noise is assumed to be 1.0 erg/s/cm^2/sr/cm^{-1}. The spectral binning-width is 10 MHz for the temperature retrievals. The red line represents the best-fit spectrum, while the blue denotes spectrum obtained with a priori temperature profile. Nadir geometry is assumed for simulations. (b) Example of the retrieved temperature profile (red line) with $1-\sigma$ retrieval error and vertical resolution, a-priori profile (blue line), and the assumed true profile (black). (c) Expected uncertainty of temperature retrieval. The sensitive region is shown as a solid line. (For interpretation of the references to color in this figure legend, the reader is referred to the web version of this article).

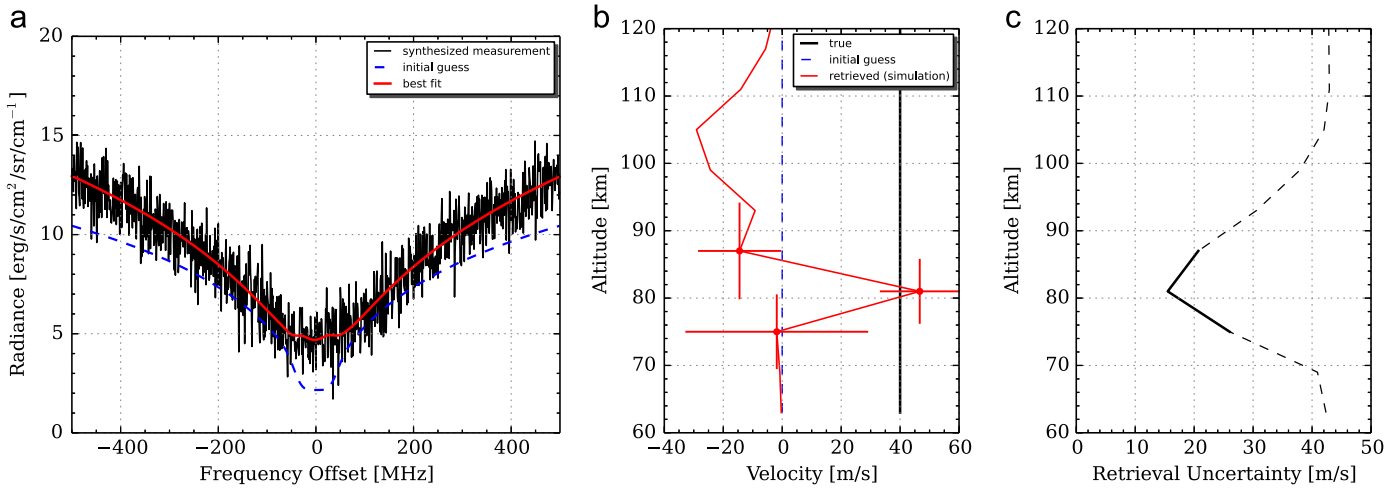

Fig. 11. Simulated wind profile retrieval for Venus. (a) Synthetic spectrum (black) of the CO_2 absorption line at R14 (971.930 cm^{-1}). The root–mean–square (RMS) noise is assumed to be 1.0 erg/s/cm^2/sr/cm^{-1}. The spectral binning-width is 1 MHz for wind retrievals. The red line represents the best-fit spectrum derived after retrieval simulation, while the blue denotes spectrum obtained with a priori profile. Limb geometry is assumed for simulations. (b) Example of the retrieved wind profile (red line), a-priori profile (blue line), and assumed true profile (black). (c) Expected uncertainty of wind retrieval. The sensitive region is shown as a solid line. (For interpretation of the references to color in this figure legend, the reader is referred to the web version of this article).

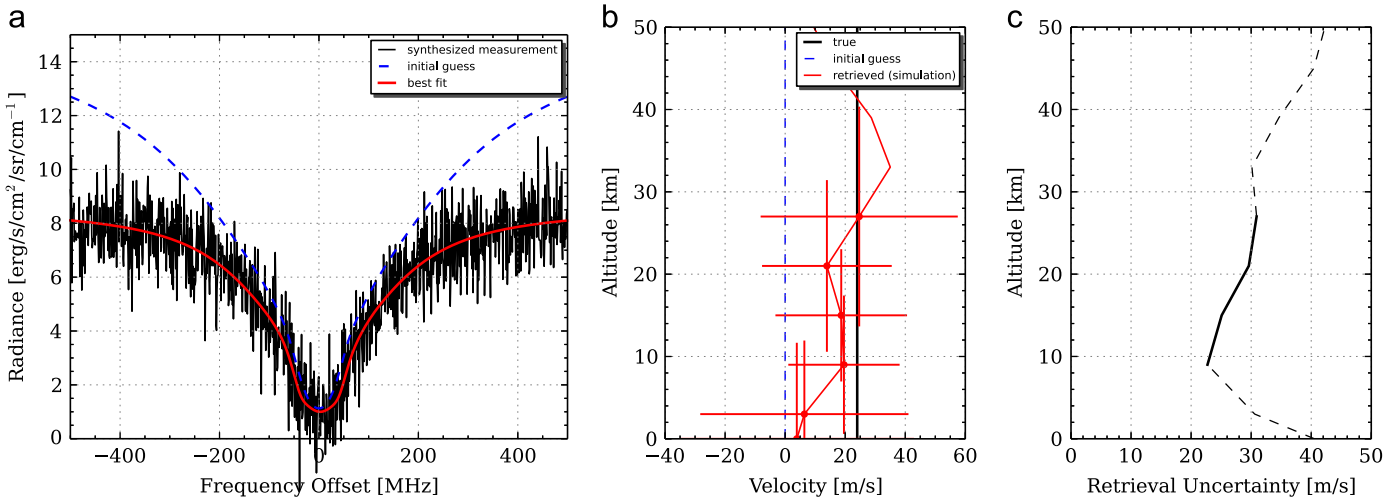

Fig. 12. Simulated wind profile retrieval for Mars. Figure format is as same as Fig. 11. (a) Synthetic spectrum (black) of the CO_2 absorption line at R14 (971.930 cm^{-1}). The root–mean–square (RMS) noise is assumed to be 1.0 erg/s/cm^2/sr/cm^{-1}. The spectral binning-width is 1 MHz for wind retrievals. The red line represents the best-fit spectrum, while the blue denotes spectrum obtained using a priori profile. Limb geometry is assumed for simulations. (b) Example of the retrieved wind profile (red line), a-priori profile (blue line), and assumed true profile (black). (c) Expected uncertainty of wind retrieval. The sensitive region is shown as a solid line. (For interpretation of the references to color in this figure legend, the reader is referred to the web version of this article).

altitude different from the submillimeter/millimeter observations (95–115 km in altitude). The sensitive altitude range of IR heterodyne, ~80 km, is of great interest as the transient region between the retrograde zonal flow in the lower atmosphere and the subsolar-to-antisolar flow in the upper atmosphere. The sensitivity can be improved with increasing the signal-to-noise ratio of the measurements.

4.5. Wind profiles on Mars

The same wind retrieval simulation is applied for Mars in Fig. 12. Fig. 12a shows the synthetic spectrum of CO_2 absorption at R14 (971.930 cm^{-1}) from limb geometry on Mars. Fig. 12b shows that the wind velocities between altitudes of 10–25 km can be resolved with 10 km vertical resolution. The derived uncertainty of the wind retrieval is 20–30 m/s, as seen in Fig. 12c. Since previous spaceborne IR measurements were unable to directly retrieve wind velocity in the lower atmosphere, IR heterodyne observations will provide instantaneous dynamic views of the Martian lower atmosphere.

4.6. Direct measurements of wind and temperature in the mesosphere

Mesospheric winds and temperature can be directly derived from the observed CO_2 non-LTE emission, as shown in Fig. 8. Line-of-sight velocity is directly obtained from the Doppler-shift of the emission line, and the temperature from Doppler width (FWHM). In contrast, the temperature is obtained by the Doppler FWHM by using the following Doppler equation (Bernath, 2005):

$$\Delta\nu_D = \frac{\nu_0}{c}\sqrt{\frac{8kT\ln(2)}{m}}, \tag{7}$$

where $\Delta\nu_D$ denotes the FWHM at the temperature T for a molecule with mass m at the observed frequency ν_0 (see Bernath, 2005). The line width of 44 MHz yields a temperature of 214 K. A Gaussian line profile was fitted to provide the line-center frequency and FWHM of the emission. The accuracies of the derived wind velocity are expected to be down to 10 m/s with 1 MHz resolution depending on fit uncertainties, uncertainties for the absolute position, uncertainties caused by the relative Doppler-shift between Earth and the target, and instrumental uncertainties (Sornig et al., 2013; Nakagawa et al., 2013). The fitting errors for the line correspond to the uncertainties of 10 m/s and 3–20 K (Sornig et al., 2013; Sonnabend et al., 2010). In contrast, previous research suggested that observed short-term variations in the Venusian mesospheric wind velocity are 60–190 m/s in time scales of hours and days (Nakagawa et al., 2013). Clancy et al. (2012) also reported significant wind deviations in the range of 20–50 m/s. Temperature in the Venusian mesosphere also have strong variability of 190–250 K, as reported by Sonnabend et al. (2012). The accuracies of wind and temperature of IR heterodyne spectroscopy are sufficient for investigating these variations in the middle atmosphere. For instance, by monitoring the wind perturbations and local heating in the middle atmosphere on Mars and Venus, the effect of gravity waves from the lower atmosphere on those of the middle atmosphere will be investigated.

4.7. Methane on Mars

We estimated the minimum detectable intensity and required integration time for detection of CH_4, H_2O_2, and the water vapor isotopic HDO/H_2O on Mars by using the well-established radiometer function shown in Eq. (5). We applied the system noise temperature T_{sys} of 4000 K at 7 μm shown in Fig. 7. It is noted, however, that the radiometer equation considers only white noise. Non-radiometric contributions such as standing waves or artifacts or the optical losses in the telescope were neglected in the present study. At 9–12 μm, the thermal radiation from Mars and Venus is observable with the IR heterodyne sensitivity. In contrast, at 7–8 μm, the lower background continuum due to the Planck curve is noted; moreover, the terrestrial atmosphere absorptions can substantially reduce the signal-to-noise ratio of the sources.

MILAHI will enable long-term integration for deep search for the Martian CH_4. Fig. 13a shows the expected absorption profiles of various mixing ratios of CH_4 at 1294.379 cm^{-1}. As seen in Fig. 13, high-spectral resolution spectra enable to remove the terrestrial atmospheric features in the spectral range by using a simple curve fit, without any radiative transfer model. This is the noteworthy advantage of IR heterodyne spectroscopy. To detect 10 ppb of CH_4, 32-h integration should be required at 15 km/s of Doppler velocity ν_D (corresponding to 0.068 cm^{-1} shifted) with 33 MHz-binning in order to increase signal-to-noise ratio ($R = 1.2 \times 10^6$) . The absorption depth of 10 ppb corresponds to 0.07 % of the

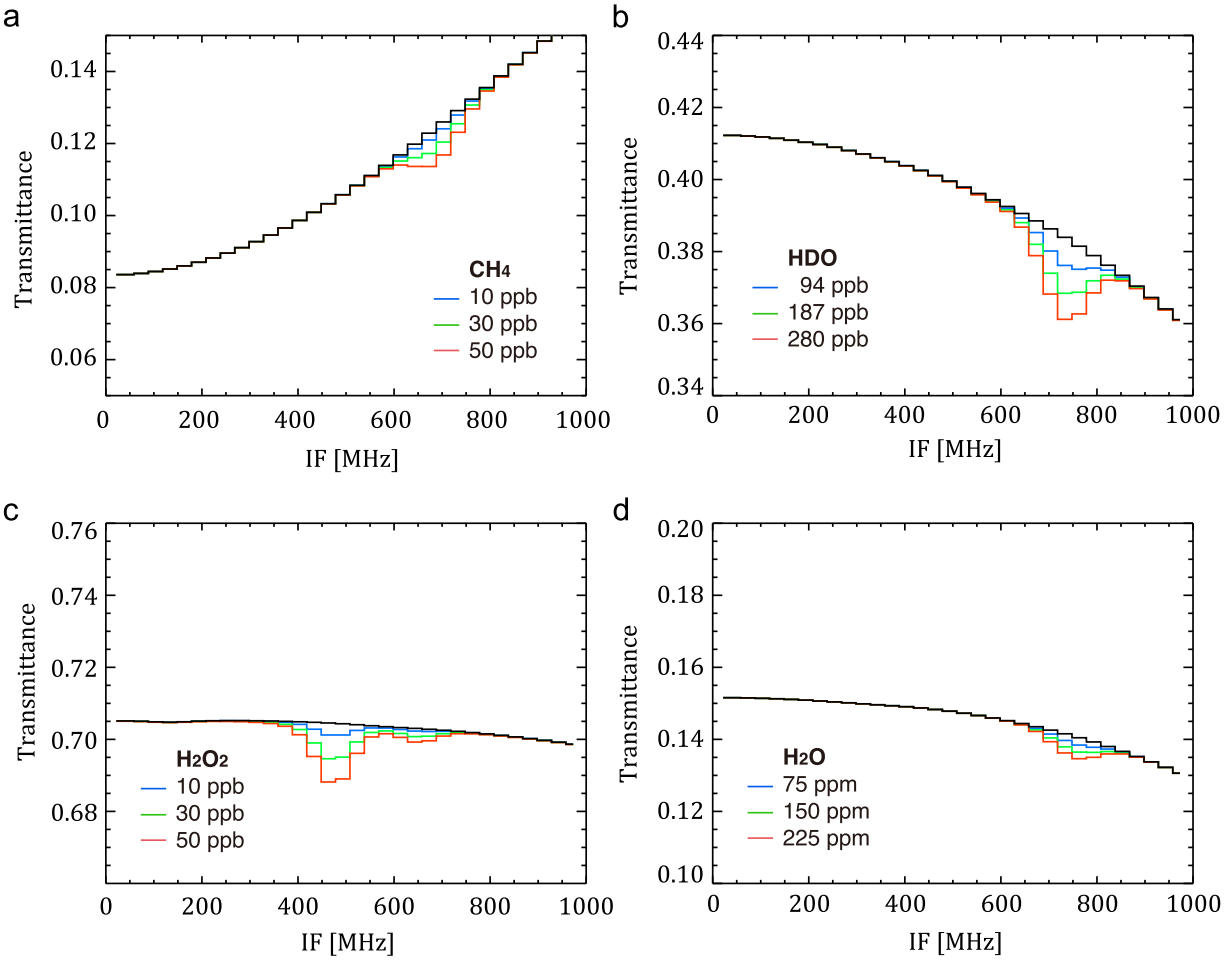

Fig. 13. Synthetic spectra of CH_4, H_2O_2, HDO, and H_2O under the assumption of Doppler velocity 15 km/s. (a) CH_4 absorption (1294.379 cm^{-1} line) by individual mixing ratios of 10, 30, and 50 ppb at the LO-frequency of 1294.337 cm^{-1}. (b) H_2O_2 absorption (1296.009 cm^{-1} line) by individual mixing ratios of 10, 30, and 50 ppb at the LO frequency of 1295.960 cm^{-1}. (c) HDO absorption (1293.289 cm^{-1} line) by individual mixing ratios of 94 (twice with respect to (wrt) Vienna Standard Mean Ocean Water (VSMOW)), 187 (four-times wrt VSMOW), and 280 ppb (six-times wrt VSMOW) at the LO position of 1293.200 cm^{-1}. (d) H_2O absorption (1296.490 cm^{-1} line) by individual mixing ratios of 75, 150, and 225 ppm at the LO-frequency of 1296.400 cm^{-1}. The spectral binning-width of these synthetic spectra is 33 MHz in order to increase signal-to-noise ratio. The black lines denote the continuum curve without absorptions.

continuum level with a Rayleigh–Jeans brightness temperature of Mars of 2.89 K at 1294.379 cm^{-1}; the physical temperature of Mars is assumed to be 288 K. We can achieve such long-term integration by using our dedicated telescope. For spatial resolution, T60 telescope (3.23 arcsec at 7.7 μm) is insufficient for resolving the source of the CH_4. We focus on the global variations at the north polar region (Geminale et al., 2011) and at the mid-latitude region in the northern hemisphere (Mumma et al., 2009). We are able to verify the previous detections by using ultra-high resolution. The time variations at various time scales are clarified to understand its source, production mechanisms, and sink. MILAHI potentially obtains vertical information of CH_4 owing to its ultra-high resolution, which could not be retrieved from previous measurements, and restricts the source and the circulation. Next, MILAHI could try to measure the resolved area with moderate resolution of 1.08 arcsec at 7.7 μm of the PLANETS 1.8 m telescope to identify the localized source.

Since the MILAHI has a capability to detect H_2O_2, comprehensive measurements of H_2O_2 and CH_4 will restrict the sink of CH_4 (Aoki et al., 2015a, 2015b). So far, H_2O_2 measurements have been performed by IRTF/TEXES (Encrenaz et al., 2004, 2008, 2012, 2015). The maps of H_2O_2 at different seasons have been investigated with an accuracy of several ppb. Fig. 13b shows the synthetic spectra for H_2O_2 with 33 MHz-binning at 1296.009 cm^{-1}. Based on our simulations, the required integration time for the detection of 10 ppb of H_2O_2 is 1.3 h when we assume the T_{sys} at 4000 K and the Doppler velocity of Mars v_D at 15 km/s. The absorption depth of 10 ppb for H_2O_2 corresponds to 0.35% of the continuum level with a Rayleigh–Jeans brightness temperature of Mars of 2.89 K at 1296.009 cm^{-1}

4.8. *Water vapor isotopes HDO/H_2O on Mars*

Based on our simulations, the required integration time for the detections of 93 ppb of HDO, corresponding to twice the concentration of VSMOW at 150 ppm of H_2O, is 15 min when we assume T_{sys} to be 4000 K and the Doppler velocity of Mars v_D to be 15 km/s with 33 MHz-binning at 1293.289 cm^{-1}. The absorption depth of 93 ppb for HDO corresponds to 0.79% of the continuum level with a Rayleigh–Jeans brightness temperature of 2.89 K. Fig. 13c shows the synthetic spectra of the HDO absorption in the Martian atmosphere.

The observability of Martian water vapor H_2O strongly depends on its transmittance surrounding the line, i.e., the highly variable terrestrial atmospheric water vapor at the weather condition at 3000 m-altitude. The same technique was applied to address the detectability of H_2O. Fig. 13d shows the synthetic spectra of H_2O absorption in the Martian atmosphere at 1296.490 cm^{-1}. When we assume a sufficient Doppler shift, v_D=15 km/s, the transmittance of the target is 0.21% with the US standard atmospheric

condition. Our result predicts that 3.62-h integration time is required to obtain the detectability for water vapor with 75 ppm. The measurements of H_2O and HDO are not exactly simultaneous. It is suggested that two-days operation time in total could provide HDO/H_2O ratio for single FOV.

With the spatial resolution of T60, we focus on the variations of HDO/H_2O at polar region with seasonal and annual scales to address the global water cycle, which is related to the sublimation–condensation process between polar caps and atmosphere. The variations of HDO/H_2O at lower and middle atmosphere is also of interest to investigate the surface-clouds-atmosphere interaction of water. Next, we perform moderate resolution mapping with the PLANETS 1.8 m telescope to investigate the localized water cycle and its evolution.

5. Conclusion

The newly developed IR heterodyne instrument, MILAHI, will explore the terrestrial atmospheres with $R > 10^6$ at 7–12 μm. The capabilities and sensitivities of IR heterodyne spectroscopy have been addressed by using modeling and prediction of radiative transfer code. Temperature profiles on Venus are obtained from 65–90 km with 3–12 K uncertainty and 5 km vertical resolution. Temperature profiles on Mars are obtained from the surface to 30 km with 4–10 K uncertainty and 10 km vertical resolution. Wind profiles on Venus are newly provided in the 80 km altitude range with 20 m/s uncertainty and 10 km vertical resolution. We also suggest that wind profiles by the IR heterodyne spectroscopy on Mars can be obtained at altitudes of 10–25 km altitude with 20–30 m/s uncertainty and 10 km vertical resolution. The local wind and temperature in the middle atmosphere can be directly derived from CO_2 non-LTE emission with 10 m/s and 3–20 K precision on both Mars and Venus mesosphere. Owing to a wide range of room-temperature-type QCLs, detections for trace gases and isotopologues can be achieved without any ambiguity for reproducing the terrestrial absorptions in the observed wavelength range. Twice the concentration of VSMOW detection of the HDO water vapor isotope on Mars can be obtained through 15-min integration, while a detectability limit of H_2O of 75 ppm is provided by 3.62-h integration time. In the case of CH_4, a detectability limit of 100 ppb can be obtained through an integration time of 32 h. Our dedicated telescopes for planetary science at Mt. Haleakalā enable long-term integration and nearly-continuous monitoring of these physical parameters. In addition, the complementary support campaign for orbiter missions such as Akatsuki around Venus, Mars Express, and MAVEN around Mars, will enhance our knowledge of planetary atmospheres.

Acknowledgments

The authors would like to thank all members of the Infrared Heterodyne spectroscopy group at Tohoku University/University of Cologne, and Theodor Kostuik, and Timothy A Livengood (NASA/GSFC) for their contributions to the work described in this paper. The authors gratefully thank all members of Institute for Astronomy (IfA), Maui, University of Hawaii (UH), for their supports to the operation at the top of Mt. Haleakalā, Hawaii. A Japanese planetary research observatory, T60, became operational and was installed at Haleakalā Observatory to replace a facility at Iitate, Fukushima, damaged by the destructive 2011 earthquake, owing to a long-standing cooperation of IfA/UH. HN expresses our thanks to Director and staff of Higashi-Hiroshima 1.5 m-telescope for their support of validation test of the instrument. This work was supported by Tohoku University Global Education and Research Center for Earth and Planetary Dynamics Program, Nagoya University, Strategic Young Researcher Overseas Visits Program for Accelerating Brain Circulation Program, Japan Aerospace Exploration Agency/Institute of Space and Astronautical Science (JAXA/ISAS), Solar-Terrestrial Environment Laboratory in Nagoya University, the Japanese Society for the Promotion of Science (JPSP) (#22740320, #25800271, #22340142, and #24403007), European Union FP7 CrossDrive Project.

References

Aoki, S., Giuranna, M., Kasaba, Y., Nakagawa, H., Sindoni, G., Geminale, A., Formisano, V., 2015a. Search for hydrogen peroxide in the martian atmosphere by the planetary Fourier spectrometer onboard Mars express. Icarus 245, 177–183.

Aoki, S., Nakagawa, H., Sagawa, H., Giuranna, M., Sindoni, G., Aronica, A., Kasaba, Y., 2015b. Seasonal variation of the HDO/H_2O ratio in the atmosphere of Mars at the middle of northern spring and beginning of northern summer. Icarus 260, 7–22.

Baron, P., Mendrok, J., Kasai, Y., Ochiai, S., Seta, T., Sagi, K., Suzuki, K., Sagawa, H., Urban, J., 2008. AMATERASU: model for atmospheric tera-hertz radiation analysis and simulation. J. NICT 55, 109.

Bernath, P., 2005. Spectra of Atoms and Molecules. Oxford University Press.

Bertaux, J.L., Vandaele, A.C., Korablev, O., Villard, E., Fedorova, A., Fussen, D., Quemerais, E., Belyaev, D., Mahieux, A., Montmessin, F., Muller, C., Neefs, E., Nevejans, D., Wilquet, V., Dubois, J.P., Hauchecorne, A., Stepanov, A., Vinogradov, I., Rodin, A., SPICAV/SOIR team, 2007. Nature 450, 646–649.

Benz, A.O., Grigis, P.C., Hungerbuhler, V., Meyer, H., Monstein, C., Stuber, B., Zardet, D., 2008. A broadband FFT spectrometer for radio and millimeter astronomy. Astron. Astrophys. 3568.

Betz, A.L., Johnson, M.A., McLaren, R.A., Sutton, E.C., 1976. Heterodyne detection of CO_2 emission lines and wind velocities in the atmosphere of Venus. Astrophys. J. 208, L141–L144.

Bradley, E.S., Robert,s, L.C., Bradford, W., Skinner, M.A., Nahrstedt, D.A., Waterson, M.F., Kuhn, J.R., 2006. Characterization of meteorological and seeing conditions at Haleakala. Publ. Astron.Soc. Pac. 118, 172–182.

Clancy, R.T., Sandor, B.J., Moriarty-Schieven, G., 2012. Thermal structure and CO distribution for the Venus mesosphere/lower thermosphere: 2001-2009 inferior conjunction sub-millimeter CO absorption line observations. Icarus 217, 779–793.

Clancy, R.T., Muhleman, D.O., Berge, G.L., 1990. Global changes in the 0-70 km thermal structure of the Mars atmosphere derived from 1975 to 1989 microwave CO spectra. J. Geophys. Res. 95, 14543–14554.

Clancy, R.T., Sandor, B.J., Moriarty-Schieven, G.H., Smith, M.D., 2006. Mesospheric winds and temperatures from JCMT sub-millimeter CO line observations during the 2003 to 2005 Mars oppositions. Second workshop on Mars atmosphere modeling and observations, February 27 - March 3.

Creasey, J.E., Forbes, J.M., Hinson, D.P., 2006. Global and seasonal distribution of gravity waves activity in Mars' lower atmosphere derived from MGS radio occultation data, Geophys. Res. Let. 33, L01803. http://dx.doi.org/10.1029/2005GL024037.

Deming, D., Espenak, F., Jennings, D., Kostuik, T., Mumma, M., Zipoy, D., 1983. Observations of the 10-μm natural laser emission from the mesospheres of Mars and Venus. Icarus 55, 347.

Encrenaz, T., Bézard, B., Greathouse, T.K., Richter, M.J., Lacy, J.H., Atreya, S.K., Wong, A.S., Lebonnois, S., Lefevre, F., Forget, F., 2004. Hydrogen peroxide on Mars: evidence for spatial and seasonal variations. Icarus 170, 424–429.

Encrenaz, T., Bézard, B., Owen, T., Lebonnois, S., Lefèvre, F., Greathouse, T., Richter, M., Lacy, J., Atreya, S., Wong, A.S., Forget, F., 2005. Infrared imaging spectroscopy of Mars: H_2O mapping and determination of CO_2 isotopic ratios. Icarus 179, 43–54.

Encrenaz, T., 2008. Search for methane on Mars: observations, interpretation on future work. Adv. Space Res. 42, 1–5.

Encrenaz, T., Greaethouse, T.K., Richter, M.J., Bézard, B., Fouchet, T., Lefèvre, F., Montmessin, F., Forget, F., Lebonnois, S., Atreya, S.K., 2008. Simultaneous mapping of H_2O and H_2O_2 on Mars from infrared high-resolution imaging spectroscopy. Icarus 195, 547–556.

Encrenaz, T., Greathouse, T.K., Lefèvre, F., Atreya, S.K., 2012. Hydrogen perioxide on Mars: observations, interpretation and future plans. Planet. Space Sci. 68, 3–17. http://dx.doi.org/10.1016/j.pss.2011.03.019.

Encrenaz, T., Greathouse, T.K., Roe, H., Richtre, M., Lacy, J., Bézard, B., Fouchet, T., Widemann, T., 2012. HDO and SO_2 thermal mapping on Venus: evidence for strong SO_2 variability. Astron. Astrophys. 543, A153.

Encrenaz, T., Greathouse, T.K., Richter, M.J., Lacy, J., Widemann, T., Bézard, B., Fouchet, T., deWitt, C., Atreya, S.K., 2013. HDO and SO_2 thermal mapping on Venus II. The SO_2 spatial distribution above and within the clouds. Astron. Astrophys. 559, A65.

Encrenaz, T., Greathouse, T.K., Lefèvre, F., Montmessin, F., Forget, F., Fouchet, T., DeWitt, C., Richter, M.J., Lacy, J.H., Bézard, B., Atreya, S.K., 2015. Astron. Astrophys. 578, A127.

Fast, K., Kostuik, T., Romani, P., Espenak, F., Hewagama, T., Betz, A., Boreiko, R., Livengood, T., 2002. Temporal behavior of stratospheric ammonia abundance and temperature following the SL9 impacts. Icarus 156, 485–497.
Fisher, D.A., 2007. Mars' water isotope (D/H) history in the strata of the north polar cap: inferences about the water cycle. Icarus 187, 430–441.
Formisano, V., Atreya, S., Encrenaz, T., Ignatiev, N., Giuranna, M., 2004. Detection of methane in the atmosphere of Mars. Science 306, 1758–1761.
Fritts, D.C., Wang, L., Tolson, R.H., 2006. Mean and gravity wave structures and variability in the Mars upper atmosphere inferred from Mars Global Surveyor and Mars Odyssey aerobraking densities. J. Geophys, Res. 111. http://dx.doi.org/10.1029/2006JA011897.
Fukunishi, H., Okano, S., Taguchi, M., Ohnuma, T., 1990. Laser heterodyne spectrometer using a liquid nitrogen cooled tunable diode laser for remote measurements of atmospheric O_3 and N_2O. Appl. Opt. 29 (18), 2722.
Fonti, S., Marzo, G.A., 2010. Mapping the methane on Mars. Astron. Astrophys. 512, A51. http://dx.doi.org/10.1051/0004-6361/200913178.
Geminale, A., Formisano, V., Sindoni, G., 2011. Mapping methane in martian atmosphere with PFS-MEX data. Planet. Space Sci. 59, 137–148.
Goldstein, J.J., Mumma, M.J., Kostuik, T., Deming, D., Espenak, F., Zipoy, D., 1991. Absolute wind velocities in the lower thermosphere of Venus using infrared heterodyne spectroscopy. Icarus 94, 45–63.
Hueso, R., Sanchez-Lavega, A., Piccioni, G., Drossart, P., Gerard, J.C., Khatuntsev, I., Zasova, L., Migliorini, A., 2008. J. Geophys. Res. 113. http://dx.doi.org/10.1029/2008JE003081.
Jakosky, B.M., Grebowsky, J.M., Luhmann, J.G., Brain, D.A., 2015. Initial results from the MAVEN mission to mars. Geophys. Res. Lett. 42. http://dx.doi.org/10.1002/2015GL065271.
Kostuik, T., Mumma, M.J., 1983. Remote sensing by IR heterodyne spectroscopy. Appl. Opt. 22 (17), 2644–2654.
Kostuik, T., 1994. Physics and chemistry of upper atmospheres of planets from infrared observations. Infrared Phys. Technol. 35, 243–266.
Kostuik, T., Buhl, D., Espenak, F., Romani, P., Bjoraker, G., Fast, K., Livengood, T., Zipoy, D., 1996. Stratospheric ammonia on Jupiter after the SL9 collision. Icarus 121, 431–441.
Kouyama, T., Imamura, T., Nakamura, M., Satoh, T., Futaana, Y., 2012. Horizontal structure of planetary-scale waves at the cloud top of Venus deduced from Galileo SSI images with an improved cloud-tracking technique. Planet. Space Sci. 60, 207–216.
Krasnopolsky, V.A., Maillard, J.P., Owen, T.C., 2004. Detection of methane in the martian atmosphere: evidence for life? Icarus 172 (537–54712), 2361–2364.
Krasnopolsky, V.A., 2012. Search for methane and upper limits to ethane and SO_2 on Mars. Icarus 217, 144–152 30.
Kuroda, T., Medvedev, A.S., Yigit, E., Hartogh, P., 2015. A global view of gravity waves in the Martian atmosphere inferred from a high-resolution general circulation model. Geophys. Res. Lett., 9213–9222. http://dx.doi.org/10.1002/2015GL066332.
Lellouch, E., Goldstein, J.J., Rosenqvist, J., Bougher, S.W., Paubert, G., 1994. Global circulation, thermal structure, and carbon monoxide distribution in Venus' mesosphere in 1991. Icarus 110, 315–339 31.
Lefèvre, F., Forget, F., 2009. Observed variations of methane on Mars unexplained by known atmospheric chemistry and physics. Nature 460, 720–723.
Livengood, T.A., Kostuik, T., Espenak, F., Goldstein, J.J., 1993. Temperature and abundances in the Jovian auroral stratosphere 1. Ethane as a probe of the millibar region. J. Geopshy. Res. 98 (E10), 18813–18822.
L´opez-Valverde, M.A., Sonnabend, G., Sornig, M., Kroetz, P., 2011. Modeling the atmospheric CO_2 10-μm non-thermal emission in Mars and Venus at high spectral resolution. Planet. Space Sci. 59, 999–1009 34.
Mahieux, A., Vandaele, A.C., Robert, S., Wilquet, V., Drummond, R., Montmessin, F., Bertaux, J.L., 2012. Densities and temperatures in the Venus mesosphere and lower thermosphere retrieved from SOIR on board Venus express: carbon dioxide measurements at the Venus terminator. J. Geophys. Res. 117, E07001. http://dx.doi.org/10.1029/2012JE004058.
Marcq, E., Bertaux, J.L., Montmessin, F., Belyaev, D., 2013. Variations of sulphur dioxide at the cloud top of Venus' dynamic atmosphere. Nat. Geosci. 6, 25–28. http://dx.doi.org/10.1038/ngeo1650 36.
Markiwicz, W.J., Titov, D.V., Ignatiev, N., Keller, H.U., Crisp, D., Limaye, S.S., Jaumann, R., Moissl, R., Thomas, N., Esposito, L., Watanabe, S., Fiethe, B., Behnke, T., Szemerey, I., Michalik, H., Perplies, H., Wedemeier, M., Sebastian, I., Boogaerts, W., Hviid, S.F., Dierker, C., Osterloh, B., Boker, W., Koch, M., Michaelis, H., Delyaev, D., Dannenberg, A., Tschimmel, M., Russo, P., Roatsch, T., Matz, K.D., 2007. Planet. Space Sci. 55, 1701–1711.
McCleese, D.J., Schofield, J.T., Taylor, F.W., Abdou, W.A., Aharonson, O., Banfield, D., Calcutt, S.B., Heavens, N.G., Irwin, P.G.J., Kass, D.M., Kleinb¨ohl, A., Lawson, W.G., Leovy, C.B., Lewis, S.R., Paige, D.A., Read, P.L., Richardson, M.I., Teanby, N., Zurek, R.W., 2008. Intense polar temperature inversion in the middle atmosphere on Mars. Nat. Geosci. 1, 745.
Medvedev, A.S., Yigit, E., Hartogh, P., Becker, E., 2011. Influence of gravity waves on the martian atmosphere: general circulation modeling. J. Geophys. Res. 116, E10004. http://dx.doi.org/10.1029/2011JE003848.
Montmessin, F., Fouchet, T., Forget, F., 2005. Modeling the annual cycle of HDO in the martian atmosphere. J. Geopshy. Res. 110, E03006. http://dx.doi.org/10.1029/2004JE002357.
Moreno, R., Lellouch, E., Forget, F., Encrenaz, T., Guilloteau, S., Millour, E., 2009. Wind measurements in Mars' middle atmosphere: IRAM Plateau de Bure interferometric CO observations. Icarus 201, 549–563.
Mumma, M.J., Villanueva, G.L., Novak, R.E., Hewagama, T., Bonev, B.P., DiSanti, M.A., Mandell, A.M., Smith, M.D., 2009. Strong release of methane on Mars in northern summer 2003. Science 323, 1041–1045.
Nakagawa, H., Hoshino, N., Sornig, M., Kasaba, Y., Sonnabend, G., Stupar, D., Aoki, S., Murata, I., 2013. Comparison of general circulation model atmospheric wave simulations with wind observations of venusian mesosphere. Icarus 225, 840–849.
Novak, R.E., Mumma, M.J., Villanueva, G.L., 2011. Measurement of the isotopic signatures of water on Mars: implications for studying methane. Planet. Space Sci. 59, 163–168. http://dx.doi.org/10.1016/j.pss.2010.06.017.
Okano, S., Taguchi, M., Fukunishi, H., 1989. Stratospheric ozone measurements with a tunable diode laser heterodyne spectrometer. Geophys. Res. Lett. 16, 551–554.
Owen, T., Maillard, J.P., de Bergh, C., Lutz, B.L., 1988. Deuterium on Mars: the abundance of HDO and the value of D/H. Science 240 (4860), 1767. http://dx.doi.org/10.1126/science.240.4860.1767.
Pätzold, M., et al., 2007. The structure of Venus' middle atmosphere and ionosphere. Nature 450, 657–660. http://dx.doi.org/10.1038/nature06239.
Peralta, J., Hueso, R., Sanchez-Lavega, A., Piccioni, G., Lanciano, O., Drossart, P., 2008. Characterization of mesoscale gravity waves in the upper and lower clouds of Venus from VEX-VIRTIS images. J. Geophys. Res. 113, E00B18. http://dx.doi.org/10.1029/2008JE003185.
Peralta, J., Luz, D., Berry, D.L., Tsang, C.C.C., Sanchez-Lavega, A., Hueso, R., Piccioni, G., Drossart, P., 2012. Solar migrating atmospheric tides in the winds of the polar region of Venus. Icarus 220, 958–970.
Rodgers, C.D., 2000. Inverse Methods for Atmospheric Sounding: Theory and Practice. World Scientific Publishing, p. 240.
Rothman, L.S., Gordon, I.E., Babikov, Y., Barbe, A., Benner, D.C., Bernath, P.F., Birk, M., Bizzocchi, L., Boudon, V., Brown, L.R., Campargue, A., Chance, K., Cohen, E.A., Coudert, L.H., Devi, V.M., Drouin, B.J., Fayt, A., Flaud, J.M., Gamache, R.R., Harrison, J.J., Hartmann, J.M., Hill, C., Hodges, J.T., Jacquemart, D., Jolly, A., Lamouroux, J., Le Roy, R.J., Li, G., Long, D.A., Lyulin, O.M., Mackie, C.J., Massie, S. T., Mikhailenko, S., Mu¨ller, H.S.P., Naumenko, O.V., Nikitin, A.V., Orphal, J., PerevalovV, J., Perrin, A., Polovtseva, E.R., Richard, C., Smith, M.A.H., Starikova, E., Sung, K., Tashkun, S., Tennyson, J., Toon, G.C., Tyuterev, V.I.G., Wagner, G., 2013. J. Quant. Spectrosc. Radiat. Transf. 130, 4–50.
Sakanoi T., Kasaba Y., Kagitani M., Nakagawa H., Kuhn J., Okano S., 2014. Development of infrared Echelle spectrograph and mid-infrared heterodyne spectrometer on a small telescope at Haleakal¯a, Hawaii for planetary observation, in: Proceedings of SPIE, 9147, Ground-based and Airborne Instrumentation for Astronomy V, 91478D. http://dx.doi.org/10.1117/12.2055877.
Sandor, B.J., Clancy, R.T., Moriarty-Schieven, G., Mills, F.P., 2010. Sulfur chemistry in the Venus mesosphere from SO_2 and SO microwave spectra. Icarus 208, 49–60.
Sandor, B.J., Clancy, R.T., Moriarty-Schieven, G., 2012. Upper limits for H_2SO_4 in the mesosphere of Venus. Icarus 217, 839–844.
Seiff, A., 1985. Models of the structure of the atmosphere of Venus from the surface to 100 km altitude. Adv. Space Res. 5, 3–58.
Smith, M.D., 2001. Interannual variability in TES atmospheric observations of Mars during 1999–2003. Icarus 167, 148–165.
Smith, M.D., Conrath, B.J., Pearl, J.C., Christensen, P.R., 2002. Thermal emission spectrometer observations of Martian planet-encircling dust storm 2001A. Icarus 157, 259–263.
Sonnabend, G., Wirtz, D., Vetterle, V., Schieder, R., 2005. High-resolution observations of martian non-thermal CO_2 emission near 10 μm with a new tuneable heterodyne receiver. Astron. Astrophys. 435, 1181–1184.
Sonnabend, G., Sornig, M., Krotz, P., Stupar, D., Schieder, R., 2008. Ultra high spectral resolution observations of planetary atmospheres using the cologne tuneable heterodyne infrared spectrometer. J. Quant. Spectrosc. Radiat. Transf. 109, 1016–1029.
Sonnabend, G., Kroetz, P., Sornig, M., Stupar, D., 2010. Direct observations of Venus upper mesospheric temperatures from ground based spectroscopy of CO2. Geophys. Res. Lett. 37, L11102. http://dx.doi.org/10.1029/2010GL043335.
Sonnabend, G., Krötz, P., Schmülling, F., Kostuik, T., Goldstein, J., Sornig, M., Stupar, D., Livengood, T., Hewagama, T., Fast, K., Mahieux, A., 2012. Thermospheric/mesospheric temperatures on Venus: Results from ground-based high-resolution spectroscopy of CO_2 in 1990/1991 and comparison to results from 2009 and between other techniques. Icarus 217, 856–862.
Sonnabend, G., Stupar, D., Sornig, M., Stangier, T., Kostuik, T., Livengood, T., 2013. A search for methane in the atmosphere of Mars using ground-based mid infrared heterodyne spectroscopy. J. Mol. Spectrosc. 291, 98–101.
Sornig, M., Livengood, T., Sonnabend, G., Kroetz, P., Stupar, D., Kostuik, T., Schieder, R., 2008. Venus upper atmosphere winds from ground-based heterodyne spectroscopy of CO_2 at 10 μm wavelength. Planet. Space Sci. 56, 1399–1406.
Sornig, M., Sonnabend, G., Stupar, D., Kroetz, P., Nakagawa, H., Mueller-Wodarg, I., 2013. Venus' upper atmospheric dynamical structure from ground-based observations shortly before and after Venus' inferior conjunction 2009. Icarus 225, 828–839.
Stangier, T., Sonnabend, G., Sornig, M., 2013. Compact setup of a tunable heterodyne spectrometer for infrared observations of atmospheric trace-gases. Remote Sens., 3397–3414. http://dx.doi.org/10.3390/rs5073397.
Stangier, T., Hewagama, T., Sornig, M., Sonnabend, G., Kostuik, T., Herrmann, M., Livengood, T., 2015. Thermal structure of Venus' nightside mesosphere as observed by infrared heterodyne spectroscopy at 10 μm. Planet. Space Sci. . http://dx.doi.org/10.1016/j.pss.2015.01.021
Stupar, D., Krieg, J., Kroetz, P., Sonnabend, G., Sornig, M., Giesen, T.F., Schieder, R., 2008. Fully reflective external-cavity setup for quantum-cascade lasers as a

local oscillator in mid-infrared wavelength heterodyne spectroscopy. Appl. Opt. 47 (16), 2993.
Taguchi, M., Okano, S., Fukunishi, H., Sasano, Y., 1990. Comparison of ozone profiles from ground-based laser heterodyne spectrometer and ozonesonde measurements. Geophys. Res. Lett. 17 (12), 2349–2352.
Tellmann, S., Pätzold, M., Häusler, B., Bird, M.K., Tyler, G.L., 2009. Structure of the Venus neutral atmosphere as observed by the radio science experiment VeRa on Venus express. J. Geophys. Res. 114, E00B36. http://dx.doi.org/10.1029/2008JE003204.
Tellman, S., Pätzold, M., Häusler, B., Hinson, D.P., Tyler, G.L., 2013. The structure of Mars lower atmosphere from Mars Express Radio Science (MaRS) occultation measurements. J. Geophys. Res. 118, 306–320. http://dx.doi.org/10.1002/jgre.20058.
Titov, D.V., Markiewicz, W.J., Ignatiev, N.I., Song, L., Limaye, S.S., Sanchez-Lavega, A., Hesemann, J., Almeida, M., Roatsch, T., Matz, K.D., Scholten, F., Crisp, D., Esposito, L.W., Hviid, S.F., Jaumann, R., Keller, H.U., Moissl, R., 2012. Morphology of the cloud tops as observed by the Venus express monitoring camera. Icarus 217, 682–701.
Usui, T., Conel, M., Alexander, D., Wang, J., Simon, J.I., Jones, J.H., 2015. Meteoritic evidence for a previously unrecognized hydrogen reservoir on Mars. Earth Planet. Sci. Lett. 410, 140–151.
Villanueva, G.L., Mumma, M.J., Novak, R.E., Radeva, Y.L., K¨aufl, H.U., Smette, A., Tokunaga, A., Khayat, A., Encrenaz, T., Hartogh, P., 2013. A sensitive search for organics (CH_4, CH_3OH, H_2CO, C_2H_6, C_2H_2, C_2H_4), hydroperoxyl (HO_2), nitrogen compounds (N2O, NH3, HCN) and chlorine species (HCl, CH3Cl) on Mars using ground-based high-resolution infrared spectroscopy. Icarus 223 (1), 11–27.
Villanueva, G.L., Mumma, M.J., Novak, R.E., K¨aufl, H.U., Hartogh, P., Encrenaz, T., Tokunaga, A., Khayat, A., Smith, M.D., 2015. Strong water isotopic anomalies in the martian atmosphere: probing current and ancient reservoirs. Science . http://dx.doi.org/10.1126/science.aaa3630.
Webster, C., Mahaffy, P., Flesch, G., Niles, P.B., Jones, J.H., Leshin, L.A., Atreya, S.K., Stern, J.C., Christensen, L.E., Owen, T., Franz, H., Pepin, R.O., Steele, A., the MSL Science Team, 2013. Isotope ratios of H, C, and O, in CO_2 and H_2O of the Martian atmosphere. Science 341, 260–263. http://dx.doi.org/10.1126/science.1237961.
Webster, C., Mahaffy, P., Atreya, S.K., Flesch, G., Mischna, M., Meslin, P.Y., Farley, K., Conrad, P., Christensen, L., Pavlov, A., Mart´ın-Torres, J., Zorzano, M., McConnochie, T., Owen, T., Eigenbrode, J., Glavin, D., Steele, A., Malespin, C., Archer, P., Sutter, B., Coll, P., Freissinet, C., McKay, C., Moores, J., Schwenzer, S., Bridges, J., Navarro-Gonz´alez, R., Gellert, R., Lemmon, M., 2014. Mars methane detection and variability at Gale crater. Science 347, 415–417.
Widemann, T., Lellouch, E., Campargue, A., 2007. New wind measurements in Venus' lower mesosphere from visible spectroscopy. Planet. Space Sci. 55, 1741–1756.
Yung, Y.L., Wen, J.S., Pinto, J.P., Allen, M., Pierce, K.K., Paulson, S., 1988. HDO in the martian atmosphere: implications for the abundance of crustal water. Icarus 76, 146–159.
Zahnle, K., Freedman, R.S., Catling, D.C., 2011. Is there methane on Mars? Icarus 212, 493–503.